Tuijin Jishu/Journal of Propulsion Technology
ISSN: 1001-4055
Vol. 45 No. 3 (2024)

Unsteady Magnetohydrodynamic Free Convective Flow Past a Vertical Porous Plate

[1]Dr. Manjula , [2]M. Hanchinal
Associate Professor, Department of Mathematics
Smt. I. S. Yadwad Government First Grade College Ramdurg.Karnataka.

Abstract: The unsteady of MHD free convection flow between past a vertical plates are studied. The different parameters values are shown in graphically.

Keywords: MHD, Porous medium.

Introduction:

Convective heat transfer in a porous media is a topic of rapidly growing interest due to its application to geophysics, geothermal reservoirs, thermal insulation engineering, exploration of petroleum and gas fields, water movements in geothermal reservoirs, etc. The study of convective heat transfer mechanisms through porous media in relation to the applications to the above areas has been made by Nield and Bejan (2006). Recently, the study of free convective mass transfer flow has become the object of extensive research as the effects of heat transfer along with mass transfer effects are dominant features in many engineering applications such as rocket nozzles, cooling of nuclear reactors, high sinks in turbine blades, high speed aircrafts and their atmospheric reentry, chemical devices and process equipments. The object of the present paper is to study the thermal radiation effect on unsteady magneto hydrodynamic flow past a vertical porous plate with variable suction. The problem is governed by the system of coupled non-linear partial differential equations whose exact solutions are difficult to obtain, if possible. So, Galerkin finite element method has been adopted for its solution, which is more economical from computational point of view. An unsteady two-dimensional laminar free convective boundary layer flow of a viscous, incompressible, electrically conducting and the chemical reaction effects on an unsteady magneto hydrodynamics free convection fluid flow past a semi-infinite vertical plate embedded in a porous medium with heat absorption is considered. The x′ - axis is taken along the vertical plate and the y′ - axis normal to the plate. It is assumed that there is no applied voltage, which implies the absence of an electric field. The transverse applied magnetic field and magnetic Reynolds number are assumed to be very small so that the induced magnetic field and the Hall Effect are negligible. The concentration of the diffusing species in the binary mixture is assumed to be very small in comparison with the other chemical species which are present, and hence the Soret and Dufour are negligible. Further due to the semi-infinite plane surface assumption, the flow variables are functions of normal distance y′ and t′ only. Now, under the usual Boussinesq's approximation, the governing boundary layer equations of the problem are:

$$\frac{\partial v}{\partial y} = 0 \quad v = v(t), \qquad (1)$$

$$\rho\left(\frac{\partial u}{\partial t} + v\frac{\partial u}{\partial y}\right) = \mu\frac{\partial^2 u}{\partial y^2} + g\beta\left(T - T_\infty\right) + g\beta^*\left(C - C_\infty\right) - \sigma B_0^2 u - \frac{v}{K^*}u\,, \qquad (2)$$

$$\rho C_p\left(\frac{\partial T}{\partial t} + v\frac{\partial T}{\partial y}\right) = k\frac{\partial^2 T}{\partial y^2} + Q\left(T - T_\infty\right) + \mu\left(\frac{\partial u}{\partial y}\right)^2, \qquad (3)$$

$$\frac{\partial C}{\partial t} + v\frac{\partial C}{\partial y} = D\frac{\partial^2 C}{\partial y^2} \qquad (4)$$

Where u′, v′ are the velocity components in x′, y′ directions respectively. t′ - the time, ρ - the fluid density, v - the kinematic viscosity, C_p - the specific heat at constant pressure, g -the acceleration due to gravity, β and β* -

the thermal and concentration expansion coefficient respectively, B_0 - the magnetic induction, α - the fluid thermal diffusivity, K′ - the permeability of the porous medium, T′ - the dimensional temperature, C′ - the dimensional concentration, k -the thermal conductivity, μ - coefficient of viscosity, D - the mass diffusivity.

The boundary conditions for the velocity, temperature and concentration fields are:

y = 0: u = Ut, T = Tw, C = Cw

$y \to \infty : u \to 0,$ (5)

Where u'_p is the plate velocity, T'_w and C'_w are the wall dimensional temperature and concentration respectively, T'_∞ and C'_∞ are the free stream dimensional temperature and concentration respectively, n′ - the constant.

Where A is a real positive constant, ε and εA are small values less than unity and V_0 is scale of suction velocity at the plate surface.

In order to write the governing equations and the boundary condition in dimension less form, the following non-dimensional quantities are introduced.

$$v = -V_0\left(\frac{V}{t}\right)^{1/2} \quad (6)$$

$$Gr = 4g\beta\frac{T_w - T_\infty}{U}, Gc = 4g\beta^*\frac{(C_w - C_\infty)}{U}, M = \sqrt{\frac{4\sigma t}{\rho}}, Ec = \frac{U^2t^2}{C_p(T_w - T_\infty)} \quad (7)$$

In view of equation (6), equations (2) - (4) reduced to the following dimensionless form.

f" +2(η + V_0)f' - (M + K)f = -Grθ – GcC, (8)

θ″ + 2(η + V_0)Prθ′ - SPrθ = -EcPrf′², (9)

C″ + 2(η + V_0)ScC′ = 0, (10)

And the corresponding boundary conditions are

f (0) =1, θ(0) = 1, C(0) = 1, f (∞) = 0, θ (∞) = 0, C(∞) = 0. (11)

The Galerkin expansion for the differential equation (7) becomes

$$C = \frac{erfc\left((\eta + V_0)\sqrt{Sc}\right)}{erfc\left(V_0\sqrt{Sc}\right)} \quad (12)$$

$$\frac{d\theta}{d\eta} = f_1(\eta, \theta, w) = w, \theta(0) = 1, \quad (13)$$

$$\frac{dw}{d\eta} = f_2(\eta, \theta, w) = -2(\eta + V_0)\Pr w - S\Pr\theta - Ec\Pr z^2, w(0) = ?, \quad (14)$$

$$\frac{df}{d\eta} = g_1(\eta, f, z) = z, f(0) = 1, \quad (15)$$

$$\frac{dz}{d\eta} = g_2(\eta, f, z) = -2(\eta + V_0)z + (M + K)f - Gr\theta - GcC \quad (16)$$

$$C_f = \frac{2\tau}{\rho U\sqrt{vt}} = -f'(0)$$

Where A'$_i$s are matrices of order n and X_i, B_i's column matrices having n − components. The solutions of above system of equations are obtained by using Thomas algorithm for velocity, temperature and concentration. Also, numerical solutions for these equations are obtained by C-program. In order to prove the convergence and stability of finite element method, the same C-program was run with slightly changed values of h and k and no significant change was observed in the values of u, T and C. Hence, the finite element method is stable and convergent.

Where $\tau = \mu\left(\frac{\partial u}{\partial y}\right)_{y=0}$ (17)

$$Nu = \frac{2q_w\sqrt{vt}}{k(T_w - T_\infty)} = -\theta'(0) \quad (18)$$

Figure 5(a) and Figure 5(b) illustrate the velocity and temperature profiles for different values of the Prandtl number Pr. The Prandtl number defines the ratio of momentum diffusivity to thermal diffusivity. The numerical results show that the effect of increasing values of Prandtl number results in a decreasing velocity (Figure 5(a)). From Figure 5(b), it is observed that an increase in the Prandtl number results a decrease of the thermal boundary layer thickness and in general lower average temperature within the boundary layer. The reason is that smaller values of Pr are equivalent to increasing the thermal conductivities, and therefore heat is able to diffuse away from the heated plate more rapidly than for higher values of P_r. Hence in the case of smaller Prandtl numbers as the boundary layer is thicker and the rate of heat transfer is reduced.

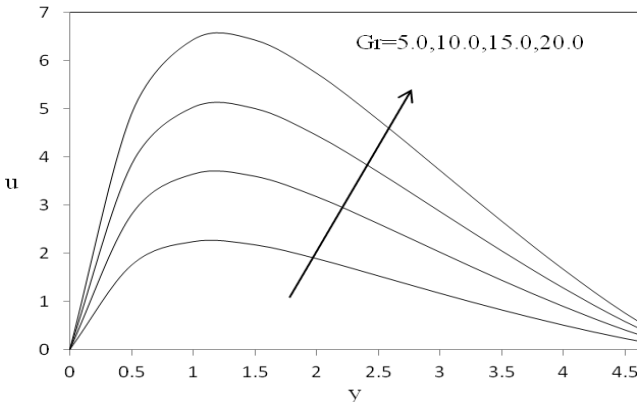

Figure 1. Velocity profile for different values of Gr

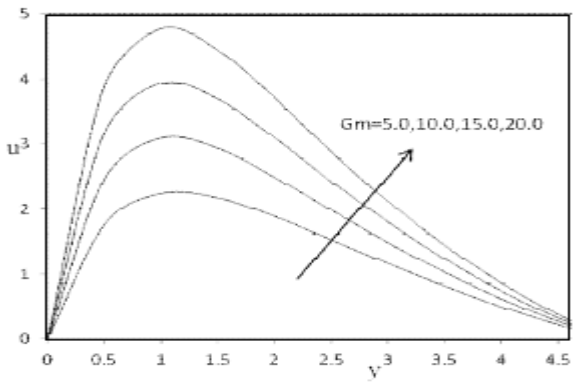

Figure 2. Velocity profile for different values of Gm

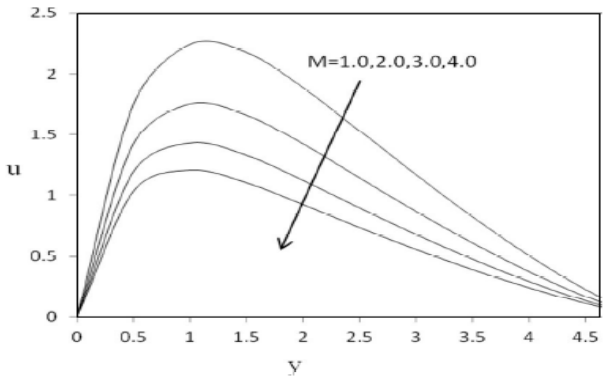

Figure 3. Velocity profile for different values of M

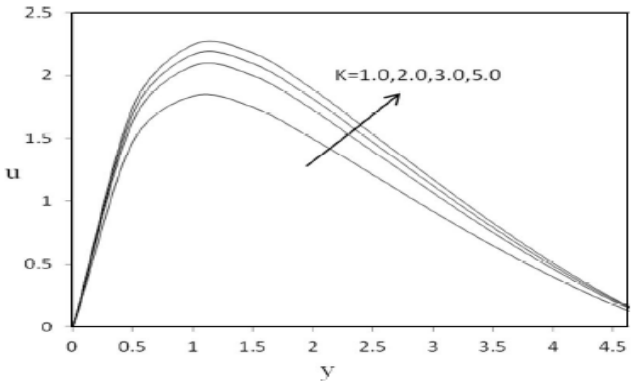

Figure 4. Velocity profile for different values of K

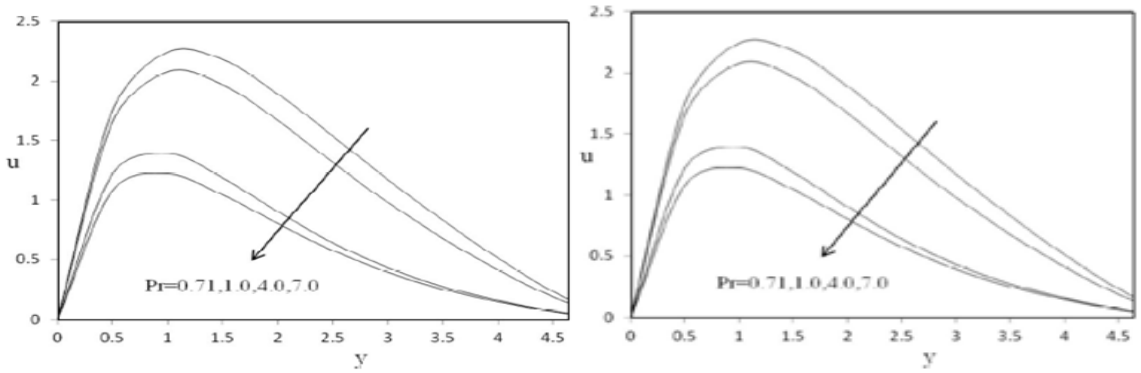

Figure 5. (a) Velocity profile for different values of Pr

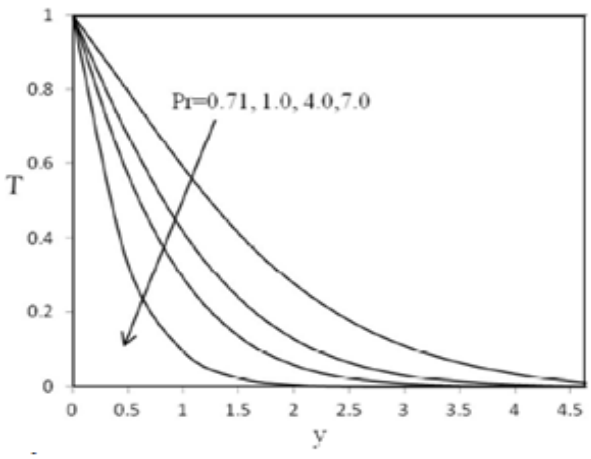

Figure5. (b) Temperature profile for different values of Pr

The influence of the Schmidt number C S on the velocity and concentration profiles are plotted in Figure 6(a) and Figure 6(b) respectively. The Schmidt number embodies the ratio of the momentum to the mass diffusivity. The Schmidt number therefore quantifies the relative effectiveness of momentum and mass transport by diffusion in the hydrodynamic (velocity) and concentration (species) boundary layers. As the Schmidt number increases the concentration decreases. This causes the concentration buoyancy effects to decrease yielding a reduction in the fluid velocity. The reductions in the velocity and concentration profiles are accompanied by

simultaneous reductions in the velocity and concentration boundary layers. These behaviors are clear from Figure 6(a) and Figure 6(b).

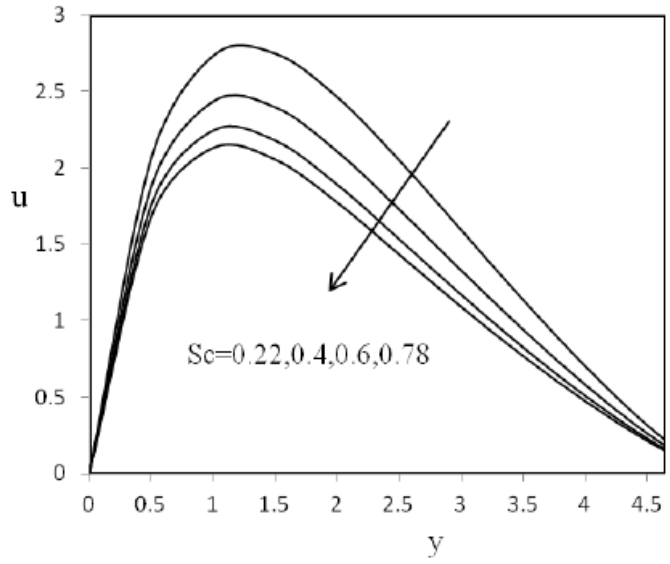

Figure 6. (a) Velocity profile for different values of Sc

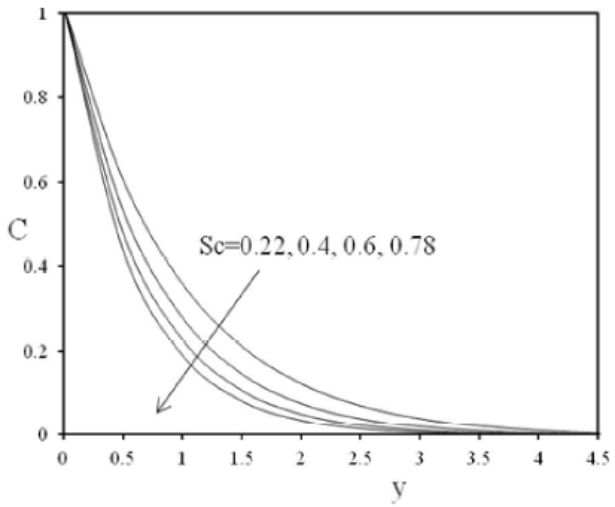

Figure 6. (b) Concentration profile for different values of Sc

Results And Discussions

Unsteady MHD flow, heat and mass transfer along an accelerated vertical porous plate in the influence of viscous dissipation, heat source and suction when the plate accelerates in its own plate is analyzed and solved numerically using Runge-kutta forth order technique .The effect of the flow parameters on the velocity and temperature distributions are presented through figures. Numerical values skin-friction coefficient and Nusselt number at the plate are derived for different values of physical parameters and presented through table.

It is observed from Figure 1 that fluid velocity decreases with the increase of the Hartmann number M, Porosity parameter K and suction velocity V0 , while it increases with the increase in Grashof number Gr modified Grashof number Gc .

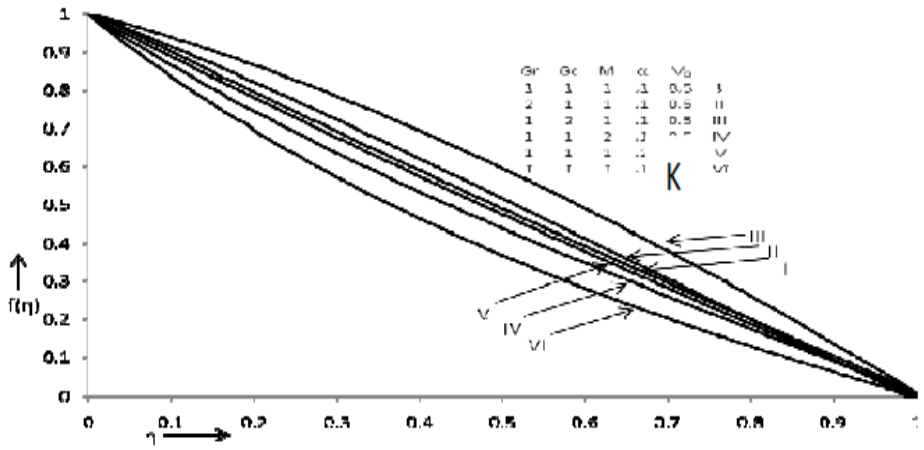

Figure 1: Velocity Profiles Versus η When Pr = 0.71, Ec = 2, S = 1 and Sc = 0.2

Figure 2 depicts that fluid temperature decreases with the increase in the Prandtl number Pr, Eckert number Ec, the Hartmann number M, heat source parameter S or suction velocity V_0.

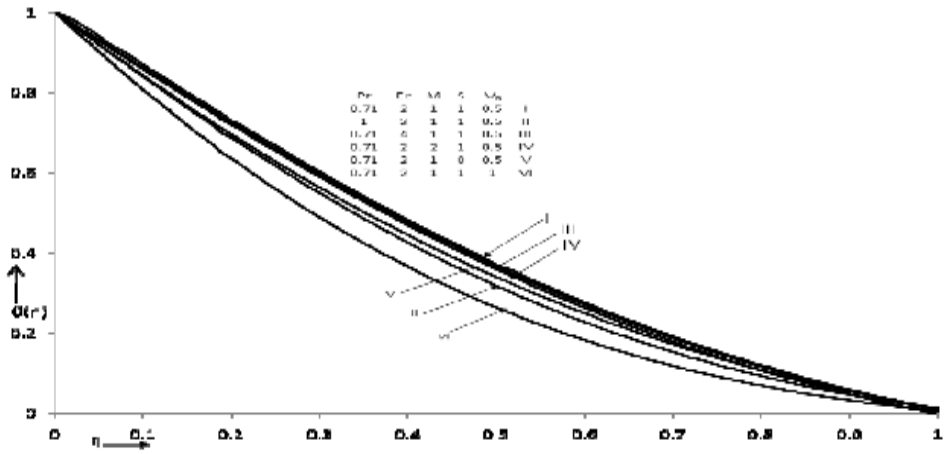

Figure 2: Temperature Profiles Versus η when Gr = 1, Gc = 1

It is observed from figure 3 that mass concentration increases with the increase in the Schmidt number.

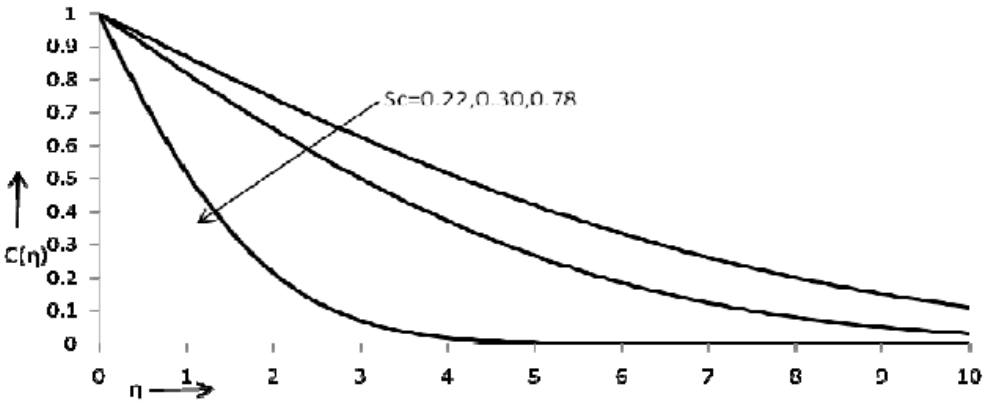

Figure 3: Concentration Profiles Versus η for Different Values of Sc with V0 = 0.5

It is seen from Table 1 that the numerical values of skin-friction coefficient increases with the increase in Prandtl Pr, Schmidt number Sc, Eckert number Ec, Hartmann number M, suction velocity V_0, while it decreases with increases in Grashof number, the modified Grashof number Gc.

The numerical values of Nusselt number increases with the increase in Prandtl Pr, Schmidt number Sc, the Grashof number Gr, the modified Grashof number Gc, suction velocity V_0, while it decreases with the increase in the Hartmann number M, the Eckert number Ec or heat source parameter S.

Table 1: Numerical Values of Nussult Number and Skin-Friction Coefficient at the Plate for Different Values of Parameters

Pr	Gr	Gc	Sc	Ec	M	K	S	V0	Nu	Cf
0.71	1	1	0.22	2	1	0.1	1	0.5	1.45525	1.07408
1	1	1	0.22	2	1	0.1	1	0.5	1.70745	1.07906
0.71	2	1	0.22	2	1	0.1	1	0.5	1.46338	0.80534
0.71	1	2	0.22	2	1	0.1	1	0.5	1.48116	0.55164
0.71	1	1	0.3	2	1	0.1	1	0.5	1.46044	1.09896
0.71	1	1	0.78	2	1	0.1	1	0.5	1.46536	1.089
0.71	1	1	0.22	4	1	0.1	1	0.5	1.4054	1.07409
0.71	1	1	0.22	2	2	0.1	1	0.5	1.4079	1.39257
0.71	1	1	0.22	2	1	0.2	1	0.5	1.47062	1.12334
0.71	1	1	0.22	2	1	0.1	0	0.5	1.65527	1.0741
0.71	1	1	0.22	2	1	0.1	1	1	2.06139	1.73714

The formulation of MHD free convective flow of an incompressible, micropolar fluid through porous medium along a semi-infinite vertical porous plate in the presence of thermal radiation field and heat source has been performed in the preceding sections. This enables us to carry out the numerical calculations for the distribution of translational velocity, microrotation, temperature and concentration across the boundary layer for various values of the parameters. In the present study we have chosen t = 1, n = 0.1, ε = 0.01, A = 1, while M, K, Gr, Gm, β, Up, Pr, R, S and Sc are varied over a range, which listed in the figure legends.

Figures (1) – (10) illustrate the velocity profiles for different values of the parameters M, K, Gr, Gm, Up, Pr, R, S and Sc. In figure – (1), the velocity profile of

micropolar fluid is plotted against y for different value of magnetic field parameter M. It is observed that the velocity increases sharply till y = 1.2, then after its velocity decreases continuously with increasing in y. It is concluded that the fluid velocity decreases with increasing magnetic field parameter M. In addition, we find that the velocity profile increases as the porosity parameter K increases, as plotted in figure – (2), Figure – (3) shows that the velocity profile for different value of Thermal Grashof number Gr. It is observed that the velocity of fluid increases with increasing the value of Gr. From figure – (4), the velocity profile of fluid (u) increases with increasing the value of Solutal Grashof number Gm. In figure – (5), we observed that due to an increase in β, there is an increase in the velocity profile. It is also observe that the velocity profile is greater for a Newtonian fluid (β > 0) with given parameters, as compared with micropolar fluids until its peak value reaches. It is also increases when Up increases as shown in figure – (6). We observe from figure – (7) that as Pr increases the velocity profile u decreases.

Table 1

Numerical values of Cf, Cm, Nu and Sh for different values of β, M, K, R, Pr, S and Sc with Gr = 3, Gm = 3, A = 1, n = 0.1, t = 1, ε = 0.01 and Up = 0.5.

β	M	K	R	Pr	S	Sc	Cf	Cm	Nu	Sh
0.1	0.1	2	1	0.71	0.01	0.4	33.54061	2.30914	0.300152	0.406216
0.3	0.1	2	1	0.71	0.01	0.4	30.91483	2.13553	0.300152	0.406216
0.5	0.1	2	1	0.71	0.01	0.4	28.48334	1.99474	0.300152	0.406216
0.1	0.3	2	1	0.71	0.01	0.4	24.41898	2.08895	0.300152	0.406216
0.1	0.1	5	1	0.71	0.01	0.4	75.30322	2.83353	0.300152	0.406216
0.1	0.1	2	2	0.71	0.01	0.4	30.63181	2.104191	0.422888	0.406216
0.1	0.1	2	1	1.2	0.01	0.4	29.00610	1.989589	0.512080	0.406216
0.1	0.1	2	1	0.71	0.03	0.4	34.21566	2.354511	0.276943	0.406216
0.1	0.1	2	1	0.71	0.01	0.6	30.14610	2.072333	0.300152	0.608523

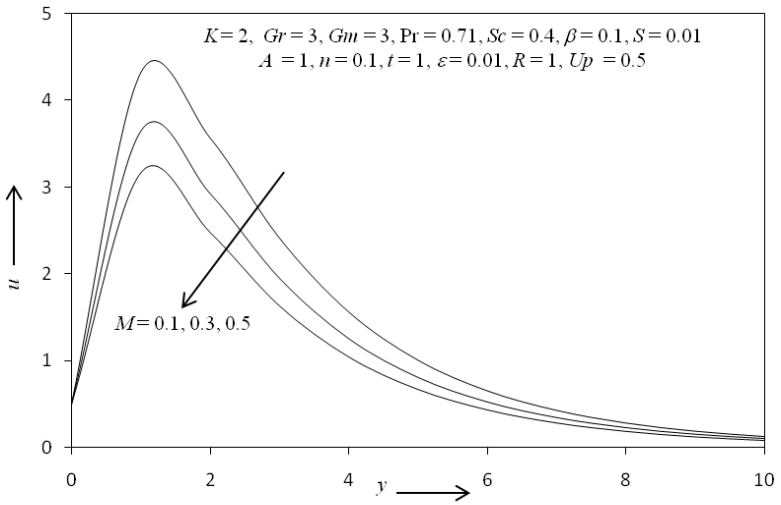

Fig. - 1: The velocity profile for different value of M.

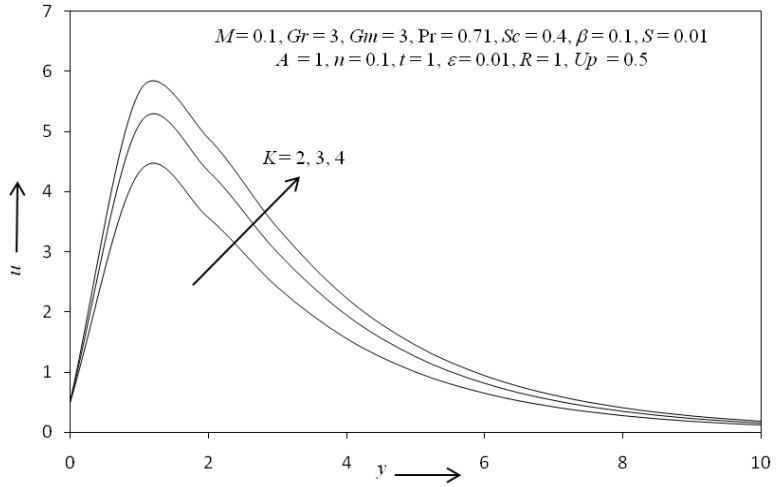

Fig. - 2: The velocity profile for different value of K.

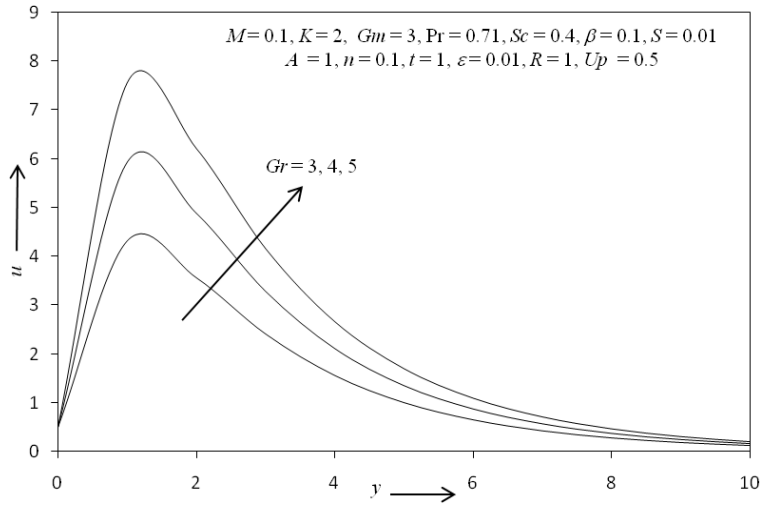

Fig. - 3: The velocity profile for different value of Gr.

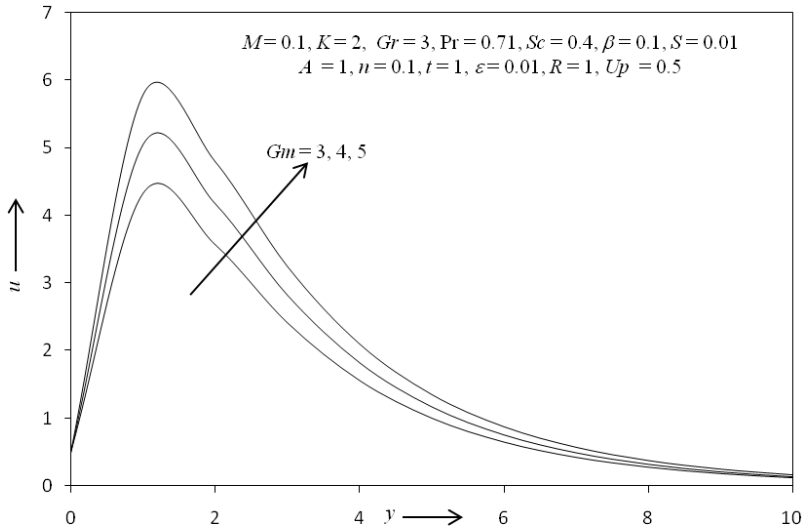

Fig. - 4: The velocity profile for different value of Gm.

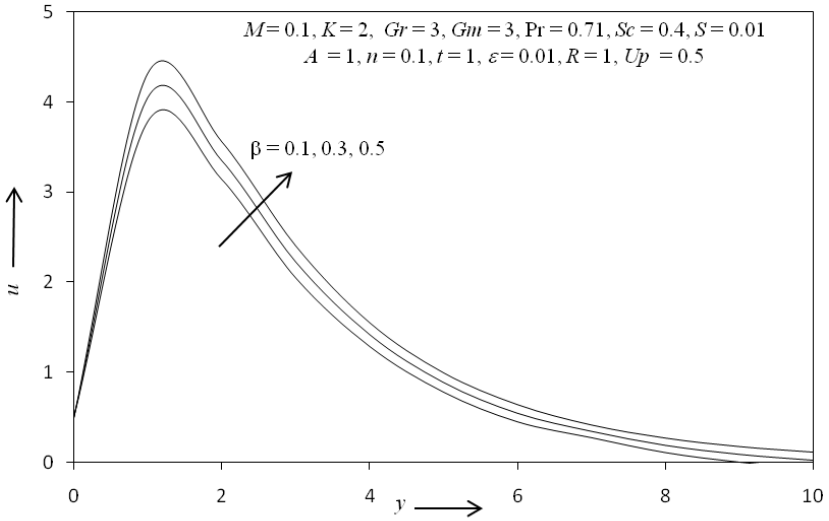

Fig. - 5: The velocity profile for different value of β.

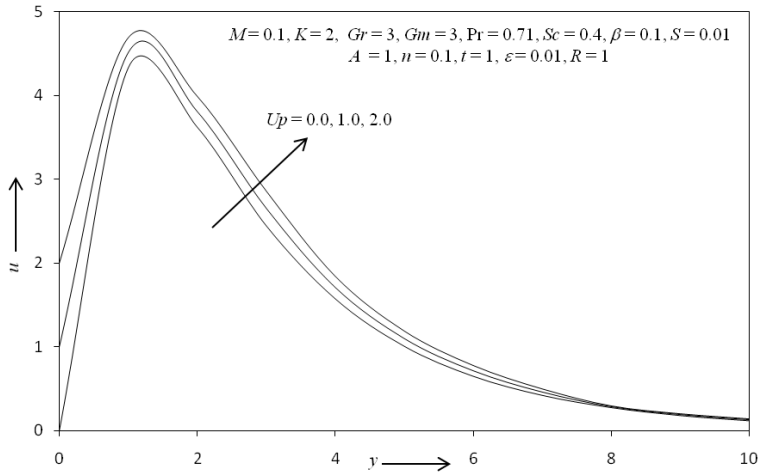

Fig. - 6: The velocity profile for different value of Up.

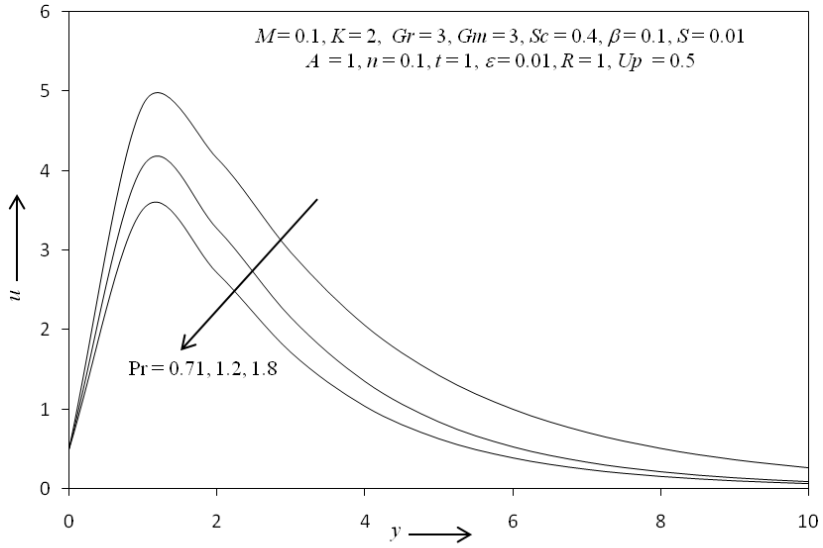

Fig. - 7: The velocity profile for different value of Pr.

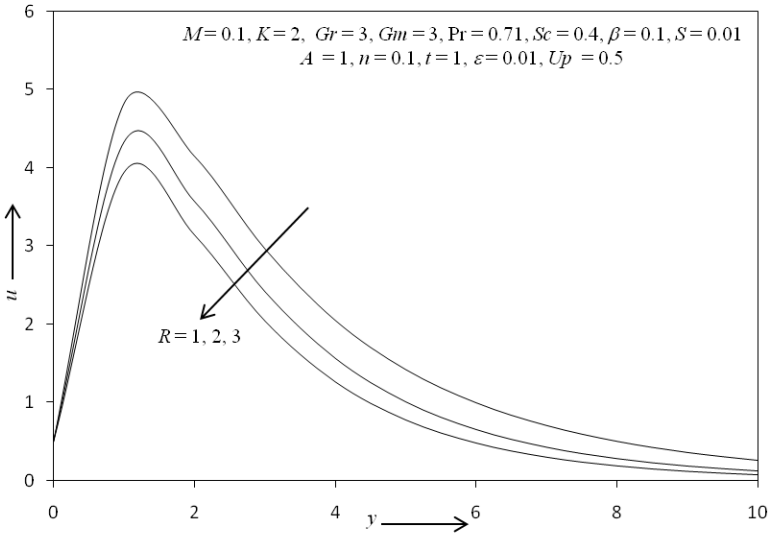

Fig. - 8: The velocity profile for different value of R.

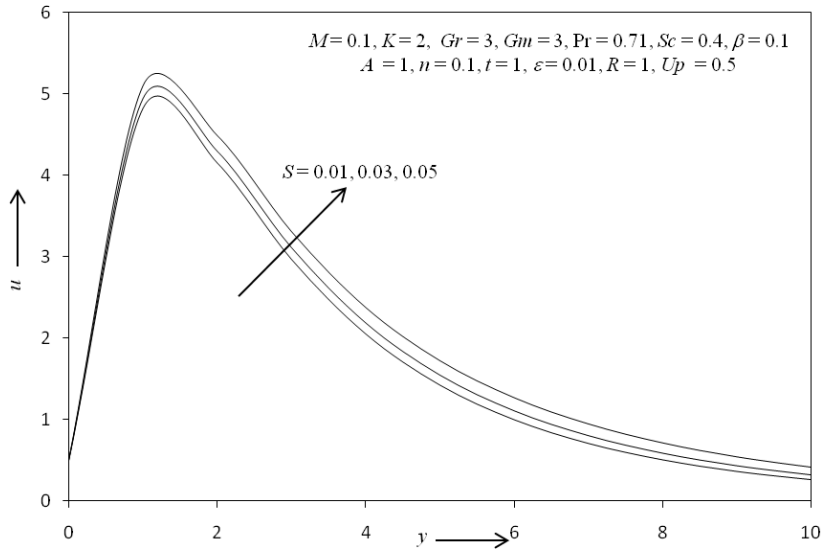

Fig. - 9: The velocity profile for different value of S.

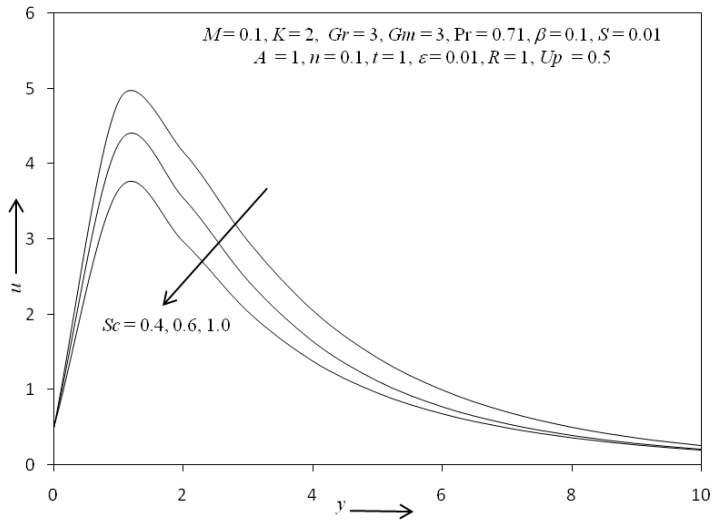

Fig. - 10: The velocity profile for different value of Sc.

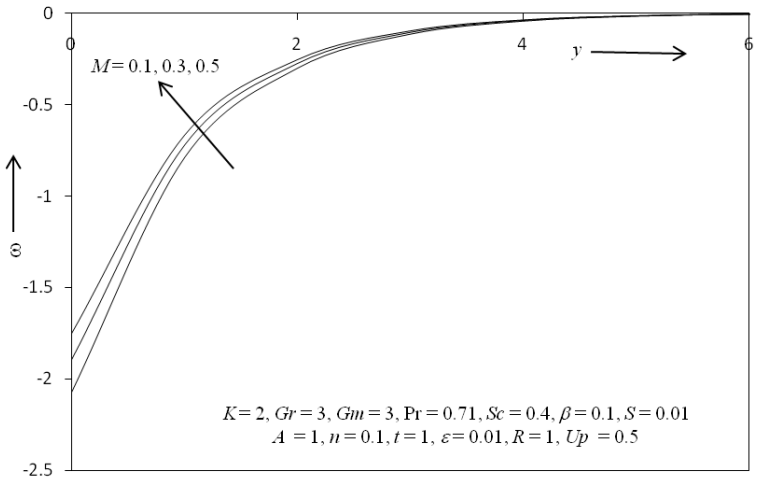

Fig. - 11: Microrotation profile for different value of M.

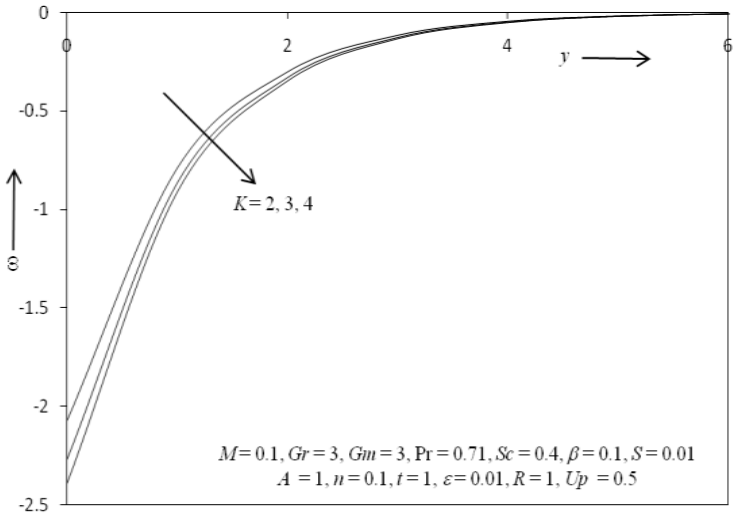

Fig. - 12: Microrotation profile for different value of K.

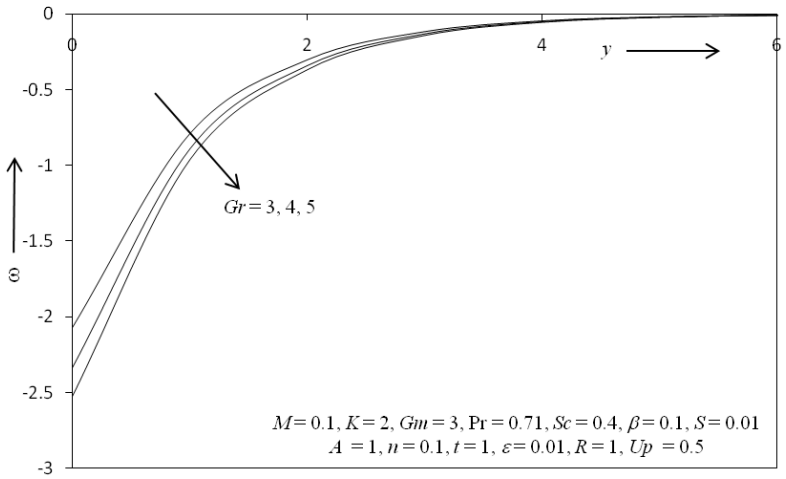

Fig. - 13: Microrotation profile for different value of Gr.

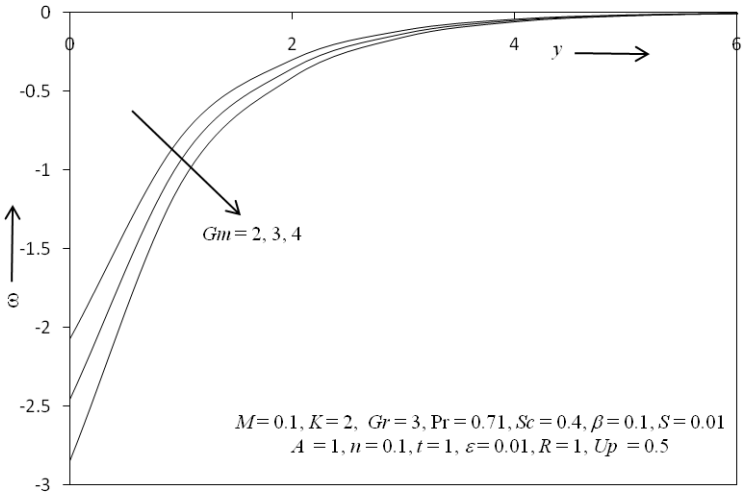

Fig. - 14: Microrotation profile for different value of Gm.

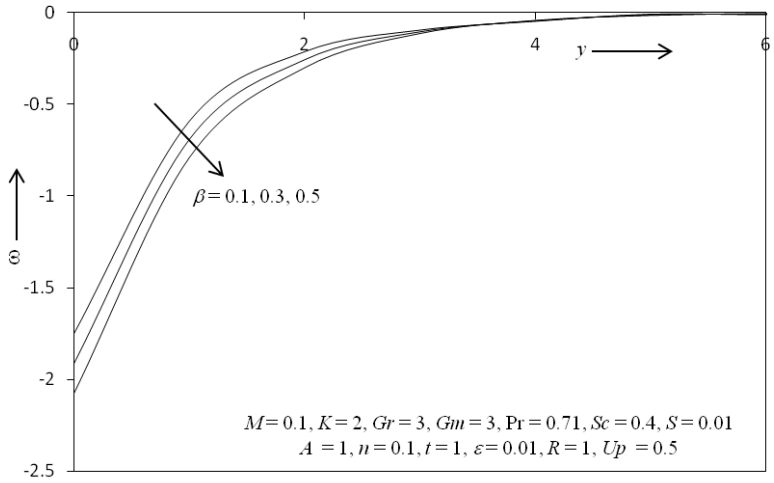

Fig. - 15: Microrotation profile for different value of β.

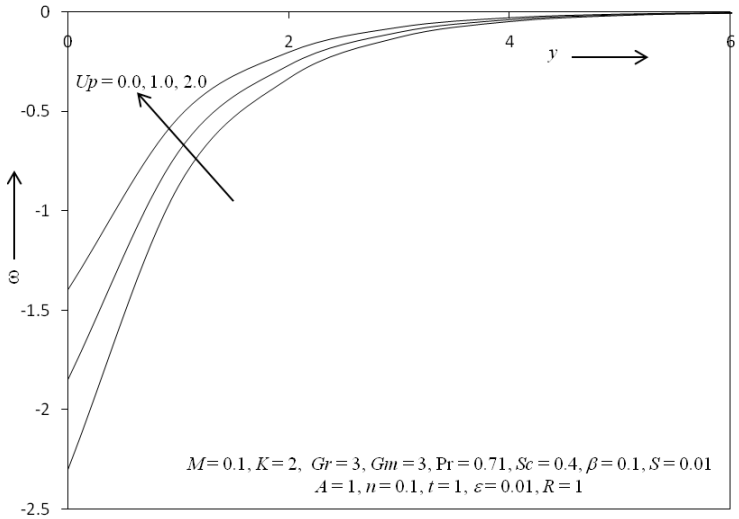

Fig. - 16: Microrotation profile for different value of Up.

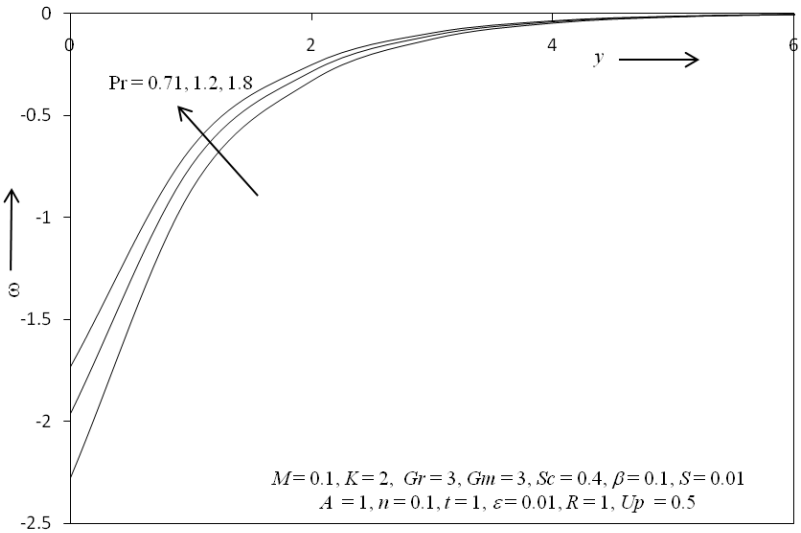

Fig. - 17: Microrotation profile for different value of Pr.

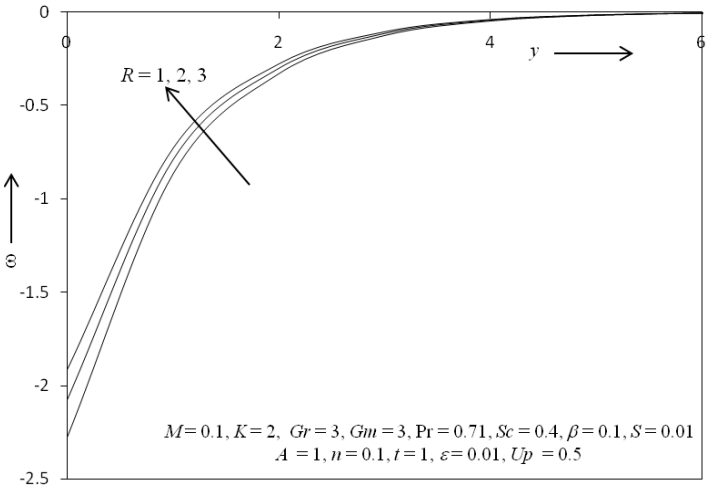

Fig. - 18: Microrotation profile for different value of R.

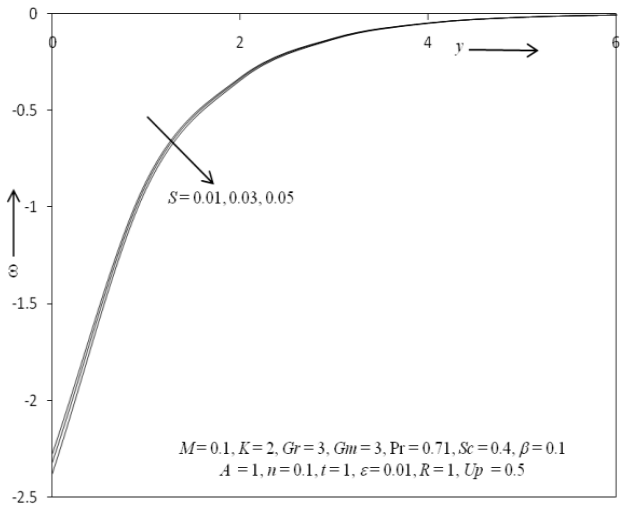

Fig. - 19: Microrotation profile for different value of S.

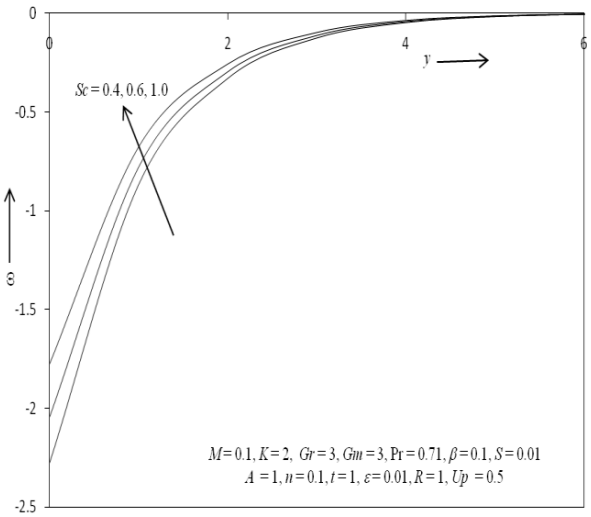

Fig. - 20: Microrotation profile for different value of Sc.

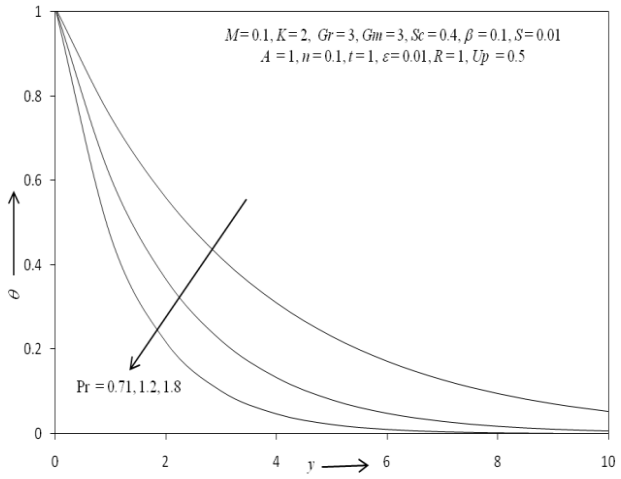

Fig. - 21: Temperature profile for different value of Pr.

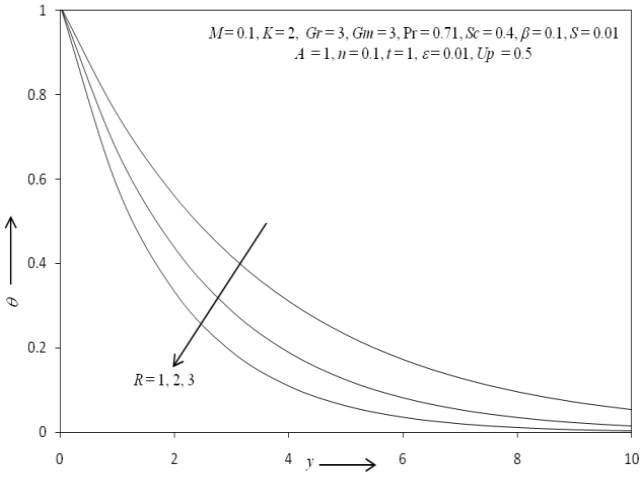

Fig. - 22: Temperature profile for different value of *R*.

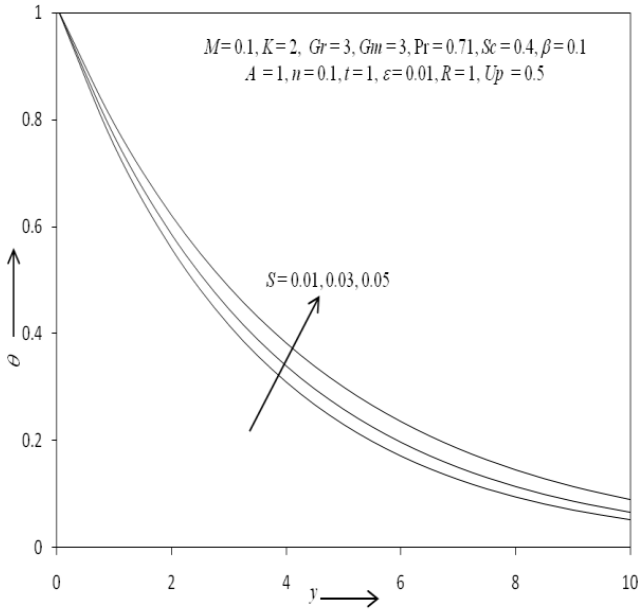

Fig. - 23: Temperature profile for different value of *S*.

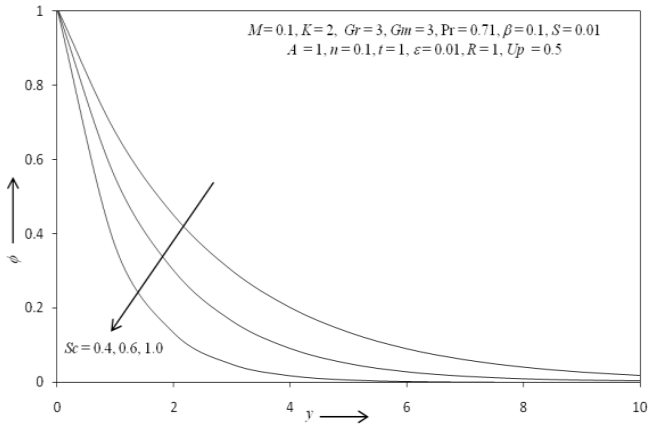

Fig. - 24: Concentration profile for different value of *Sc*.

A	M	N	Pr	−θ ′(0)		
				Liu[20]	Ishak[18]	Present
0	0	0	0.72		0.8086	0.808631
			1		1.0000	1.000000
			3		1.9237	1.923683
			6.7	3.00027	3.0003	3.000272
0	1	0	0.7	0.689699	0.6897	0.689712
			1	0.892147	0.8921	0.892147
			10	3.61699	3.617	3.616992
1	0	0	0.7		1.0834	1.083386
			7		3.7682	3.768235
1	1	0	0.7		1.0500	1.049986
			7		3.7164	3.716467
1	1	1	0.7			0.708645
			1			0.867918
			3			1.608920
			7			2.561119

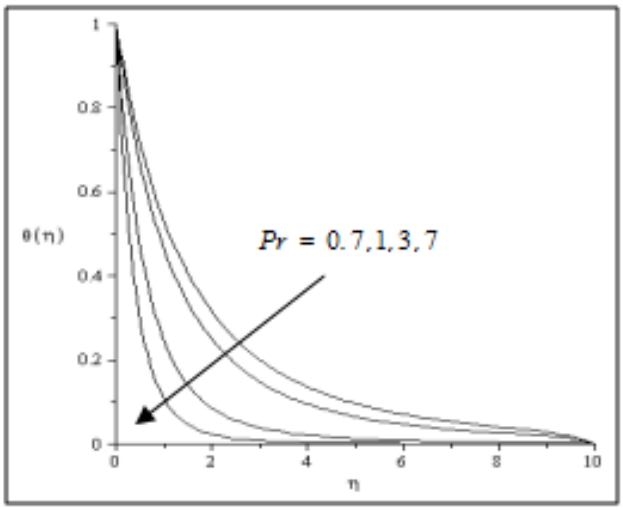

Fig. 25 Temperature profiles for various values of Pr when M = 1, N = 1 and A = 1

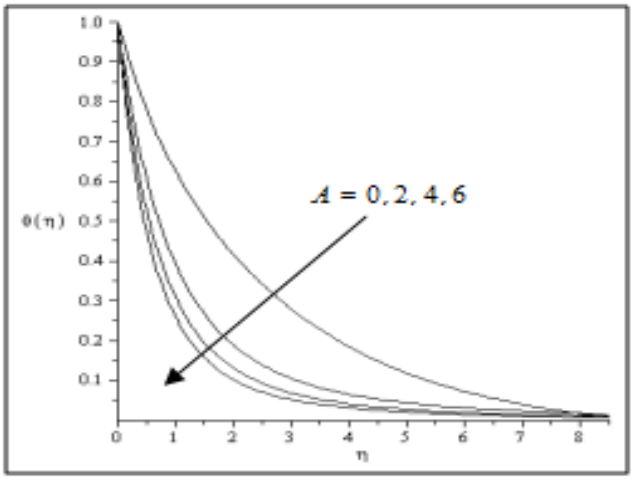

Fig. 26 Temperature profiles for various values of A when M = 1, Pr = 1 and N = 1

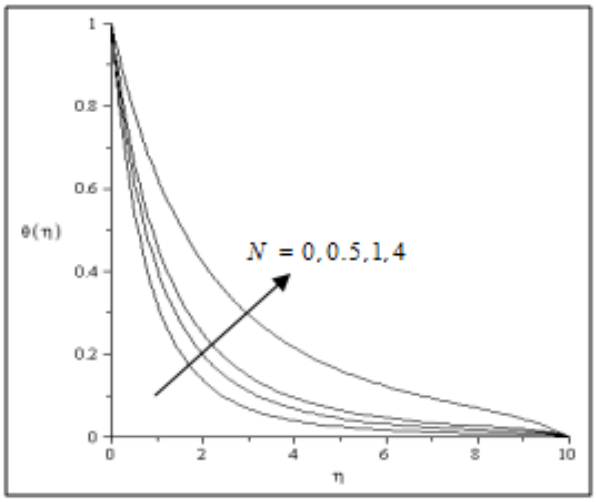

Fig. 27 Temperature profiles for various values of N when M = 1, Pr = 1 and A = 1

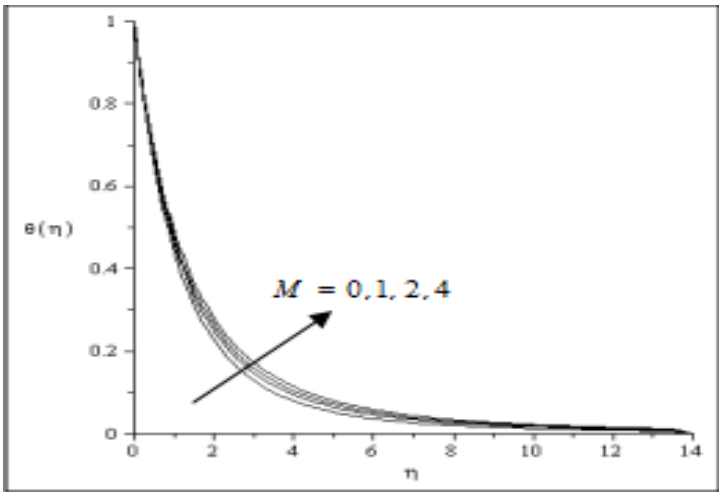

Fig. 28 Temperature profiles for various values of M when A = 1, Pr = 1 and N = 1

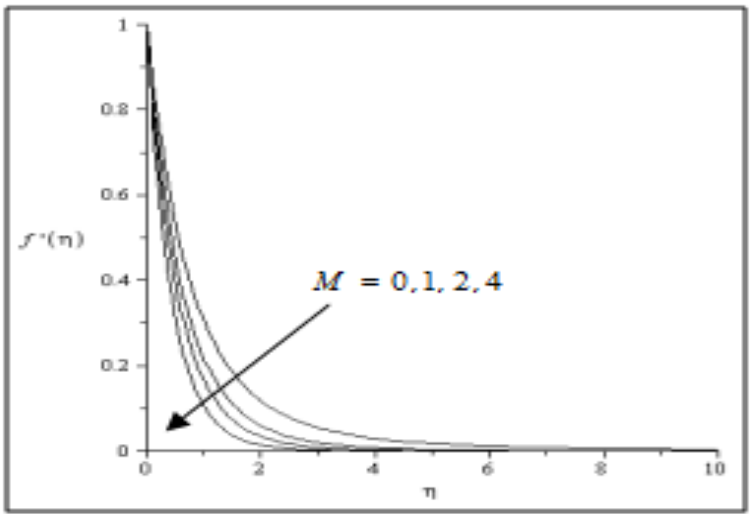

Fig. 29 Velocity profiles for various values of M when A = 1, Pr = 1 and N = 1

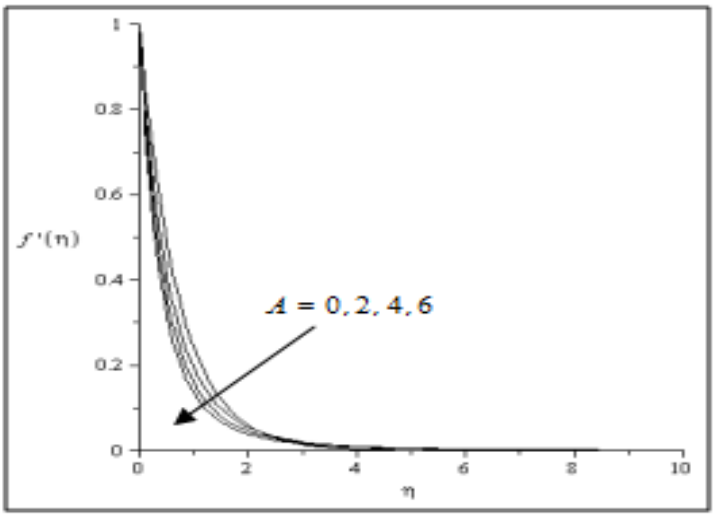

Fig. 30 Velocity profiles for various values of A when M = 1, Pr = 1, and N = 1

Numerical calculations have been carried out for different values of v0, Sr, Du, Da, M and for fixed values of Pr, Sc, Gr, Gm, Re and Fs. The value of Pr is taken to be 0.71 which corresponds to air and the value of Sc is chosen to represent hydrogen at 25^0 C and 1 atm. Due to free convection problem positive large values of Gr = 12 and Gm = 6 are chosen. The value of Re is kept 100 and Fs equal to 0.09. The values of Dufour number and Soret number are chosen in such a way that their product is constant provided that the mean temperature Tm is kept constant as well. However, the values of v0, Da and M are chosen arbitrarily. The numerical results for the velocity, temperature and concentration profiles are displayed in Figs. 3–5.

The effects of suction parameter on the velocity field are shown in Fig. 3(a). It is seen from this figure that the velocity profiles decrease monotonically with an increase of suction parameter indicating the usual fact that suction stabilizes the boundary layer growth. The effects of suction parameter on the temperature and concentration field are displayed in Fig. 3(b) and Fig. 3(c) respectively. From Fig. 3(b) we see that the temperature decreases with an increase of suction parameter. From Fig. 3(c) we observe that the concentration increases with an increase

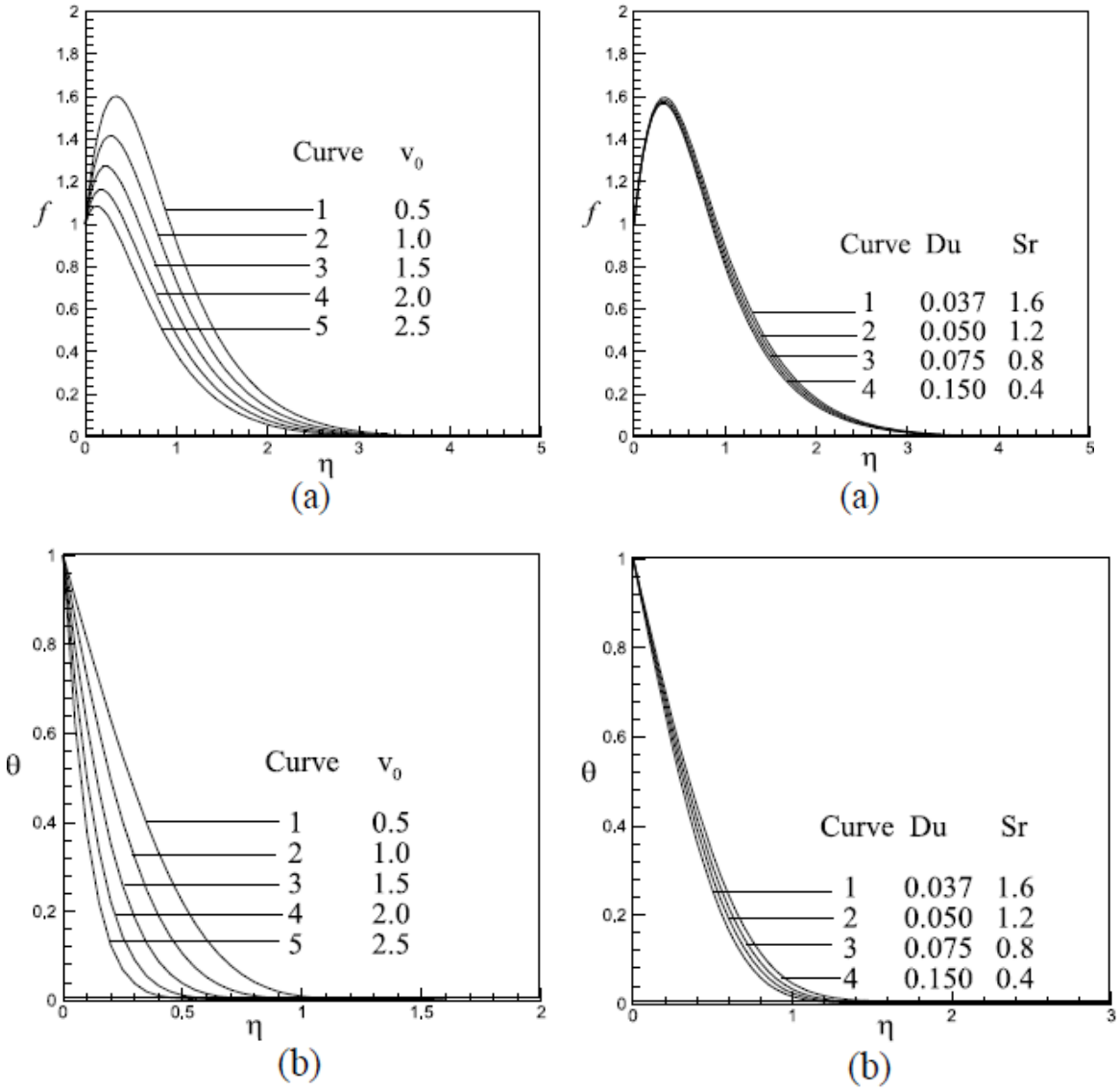

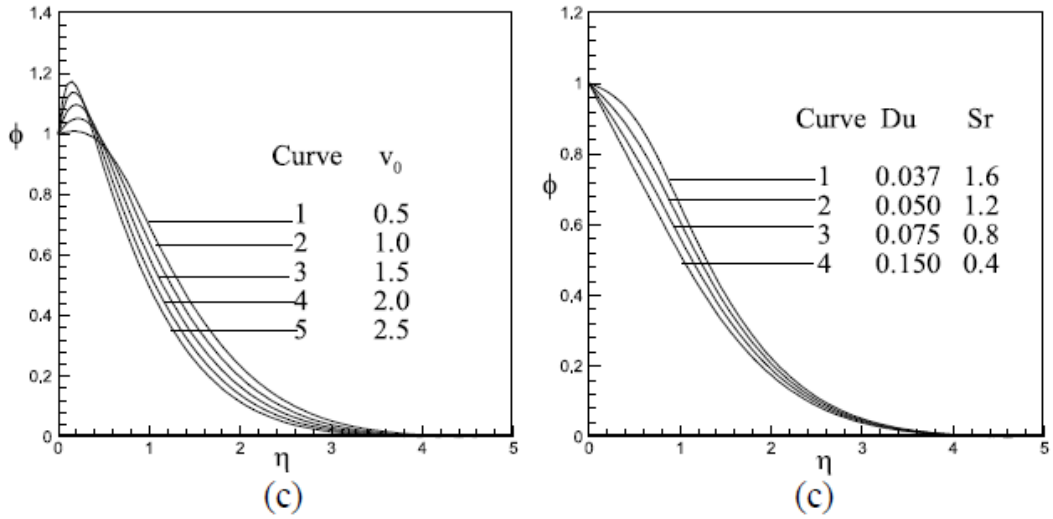

Fig. 31. (a) Velocity, (b) temperature, and (c) concentration profiles for different values of v0 for Sr = 2.0, Du = 0.03, Da = 0.5 and M = 0.3.

Fig. 4. (a) Velocity, (b) temperature, and (c) concentration profiles for different values of Du, Sr for v0=0.5, Da = 0.5 and M = 0.3.

of suction parameter close to the wall (approx. $\eta \leq 0.50$) whereas for $\eta \geq 0.50$, the concentration decreases with an incraese of suction parameter. Sucking decelerated fluid particles through the porous wall reduce the growth of the fluid boundary layer as well as thermal and concentration boundary layers.

The effects of Soret and Dufour numbers on the velocity field are shown in Fig. 4(a). We observe that quantitatively when $\eta = 1.5$ and Sr decreases from 1.6 to 1.2 there is 6.25% decrease in the velocity value, whereas the corresponding decrease is 5.87%, when Sr decreases from 0.8 to 0.4. The effects of Soret and Dufour numbers on the temperature field are shown in Fig. 4(b). We observe that quantitatively when = 0.80 and Sr decreases from 1.6 to 1.2 there is 27.56% increase in the temperature value, whereas the corresponding increase is 23%, when Sr decreases from 0.8 to 0.4. The effects of Soret and Dufour numbers on the concentration field are shown in Fig. 4(c). We observe that quantitatively when $\eta = 1.0$ and Sr decreases from 1.6 to 1.2 there is 7.64% decrease in the concentration value, whereas the corresponding decrease is 8.90%, when Sr decreases from 0.8 to 0.4.

The effects of Darcy parameter and magnetic field parameter on the velocity field are shown in Fig. 5. This figure shows that velocity increases with the increase of Darcy number. For large Darcy number, porosity of the medium increases, hence fluid flows quickly. We also see that velocity profiles decrease with the increase of magnetic effect indicating that magnetic field tends to retard the motion of the fluid. Magnetic field may control the flow characteristics.

Finally, the effects of Soret and Dufour numbers on the local Nusselt number and local Sherwood number are shown in Table 1. The behavior of these parameters is self-evident from the Table 1 and hence they will not discuss any further due to brevity.

Table 1. Numerical values of Nu and Sh at v0 = 0.5, Da = 0.5, M = 0.3

Sr	Du	Nu	Sh
2.0	0.03	1.934325	-0.086492
1.0	0.06	1.652241	0.315615
0.5	0.12	1.541984	0.468128

0.4	0.15	1.517881	0.496002
0.2	0.30	1.450355	0.549515
0.1	0.60	1.364561	0.575236

The solutions obtained in (13) and (14) describing the present problem are discussed graphically considering $\frac{\sigma B_0^2 h^2}{\upsilon\rho} = 2$ (fixed), a part of Magnetic Hartmann number $M = \frac{\sigma B_0^2 \cos^2\theta h^2}{\upsilon\rho}$ and supposing θ = 0, $\frac{\pi}{6}$, $\frac{\pi}{4}, \frac{\pi}{3}, \frac{\pi}{2}$. When θ = 0, the magnetic field is perpendicular to the direction of the flow of the fluid and when $\theta = \frac{\pi}{6}$ the magnetic field is parallel to the flow field, and in this case magnetic field has no effect on temperature field. The variation of temperature field in respect of changing time t, the Prandtl number P_r and decay factor n (> 0) has been shown through the figures (1) - (3). As $\theta = \frac{\pi}{2}$ i.e. M = 0, makes the values of the velocity profile infinite, it is not shown in the figure. For other standard values of θ, the velocity distribution profiles are shown for different values of t, P_r, and n. Here, we have assumed the adiabatic plate at y′ = +h(i.e.y = 1) and temperature function plate at. y′ = −h(i.e.y = −1) . A quantitative discussion has been given below in a nutshell for each of the values of θ and through every figure. Figure (1) has been obtained by plotting the temperature distribution T against y for t = .1, .5, 1, 4 at n = 1, P_r = 0.025 (fixed). It is observed that as t increases the values of T increases. For small time the temperature function plate receives higher temperature than the adiabatic plate, whereas for large time each plate acquires same temperature. Though not shown in the picture, the calculated value obtained for T, are almost similar for t = 3, 4, 5. Figure (2) of temperature field is obtained for various values of decay factor n (n =1, 5, 10, 15) when t = 0.1 and P_r = 0.025. It is seen that the values of temperature distribution decreases towards the adiabatic plate. An increase in the values of n leads to the increase in the values of T to a certain limit. After that it ceases to increases. In this case the effect of adiabatic plate is significant. Figure (3) has been obtained by plotting the temperature distribution T against y at the Prandtl number r P =1, 0.5, 0.25, 0.125 and at n = 5 and t = 0.1. This figure shows the significant effect of the Prandtl and adiabatic plate. For the fluid whose Prandtl number is .025, the temperature distribution is less affected, though it has a tendency towards the adiabatic plate. For other fluids that have been considered in this work, the effect of temperature distribution inside the channel increases as P_r increases towards the temperature function plate. But towards the adiabatic plate all values tends to 0. The results for the velocity u for θ = 00 (M = 2), are shown in figures (4) to (6). Figure (4) has been obtained for different time t = 0.1, 0.5, 1, 4 at P_r = 0.025 and n = 5. It is seen that for small time u increases when t increases with indication of no rise of temperature towards the adiabatic plate. But for large time this increasing rate becomes negligible, and also no difference of rise of temperature between the two plates. The flow distribution is highest at the middle of the channel at large time. Figure (5) has been obtained for different values of n, keeping t and P_r fixed at 1 and 0.025 respectively. Here we find that though there cannot be seen any effect of the adiabatic plate the effect of increase of n can be observed. But, it cannot go further. For values of n greater than 15, the values of u are almost equal leading to fully developed situation. Considering n = 5, t = 1 and varying P_r at 0.025, 0.125, 0.25, we obtained the graphs for velocity profiles as shown in the figure (6). It is seen that as P_r increases, the values of u decreases. The flow distribution for any fluid at and near the plate is almost same, but different at the middle of the channel only. We failed to get the flow distribution for the fluid whose P_r = .71, 1 due to the presence of the square root domain error. The results for the flow field u for θ = 30^0 are shown through the figures (7) - (9). Here, it is found that the velocity profiles are similar to the figure (4) for t = 0.1, 0.5, 1, 4, and P_r = 0.025 and n = 5. However, in each case the values of u are greater than got in figure 3-4 for θ = 0^0. This shows the effect of M. Supposing n = 1, 10, 15, 25, and P_r = 0.025, t = 1, we obtained the figure (8). It is seen that the velocity profiles found in the figures (5) and (8) have their similarity in their origin. Exception is that these values are greater than the values

got in (5). Figure (9) has been obtained considering t = 1, n = 5, and P_r = .025, .125, .25. This figure is similar to the figure (6). But these values are higher than the values got in figure (6). Moreover, the effect of adiabatic plate can be observed for high Prandtl number. The investigation cannot be carried out for = .71 P_r and 1 due to the domain error appeared in square roots terms. Also clear effect of Prandtl number is depicted rather than the effect of isomorphic plate. Figures (10) - (12) have been obtained by placing the magnetic field at $\theta = 45^0$. In all these three figures an excellent effect of magnetic number has been seen. The velocity distribution found in each figure is parabolic at positive quadrant of the rectangular axes, for different values of t, P_r and n though the variation of t, n and P_r at different stages can - not be neglected. However, in this case each obtained values are higher than the values got earlier for M = 2, 1.5. Considering the magnetic field at an angle $\theta = 60^0$ to the horizontal direction, we have found the velocity distribution as shown in figures (13) - (15). Figure (13) has been obtained by assuming P_r = 0.025, n = 5 and t = 0.1, 0.5, 1, 3. In the figure it is found that the velocity profiles are parabolic in the positive quadrant of rectangular axes. The values are higher than the values got in figures (4) and (10). For small times the flow distribution near the two plates are different. The figure (14) is for n = 1, 5, 10, 20, and for fixed values of P_r = 0.025 and t = 1. Here, it is seen that the fluid velocity is maximum at y = 0, and as n increases u also increases up to a certain limit. The flow distribution differs slightly for large n. The figure (15) has been obtained varying only P_r, and assuming t = 1 & n = 1. It is significant to note that for P_r= .71, & 1, the velocity fields can be drawn comfortably, which we failed to have for $\theta = 0^0, 30^0, 45^0$. The effect of adiabatic plate is clearly visigible in this case. The values of velocity distribution are higher than in each case than got for $\theta = 0^0, 30^0, 45^0$.

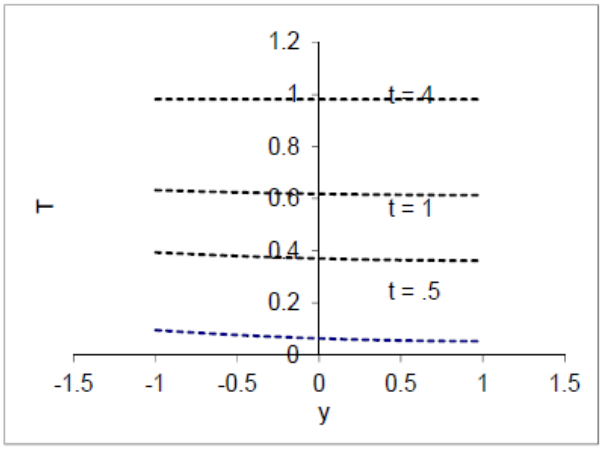

Figure 1: T versus y for n = 1, Pr = .025 at different t

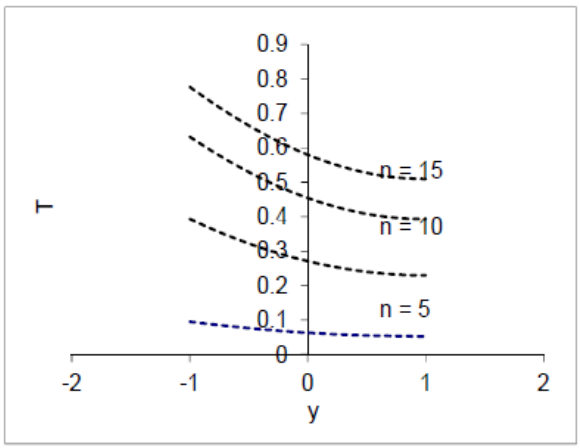

Figure 2: T versus y for Pr = .025, t = .1 at different n

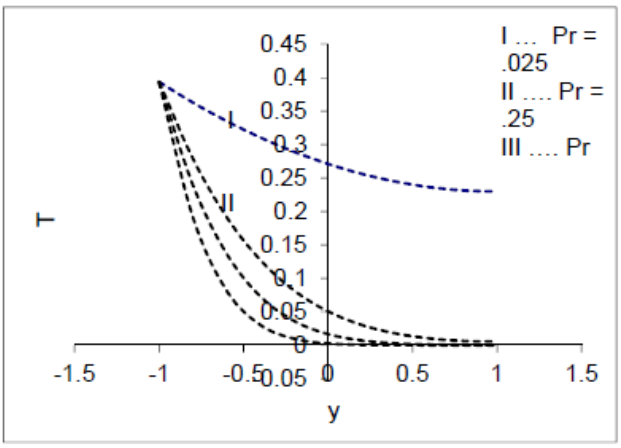

Figure 3: T versus y for n = 5, t = .1 at different Pr.

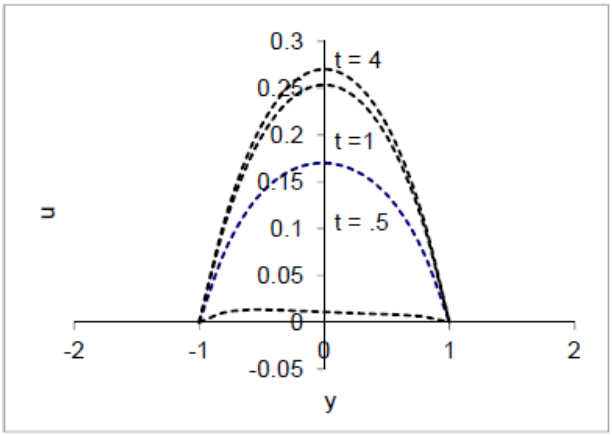

Figure 4: u versus y for M = 2 (θ = 0^0), n = 5, Pr = .025; at t = .1, .5, 1,4

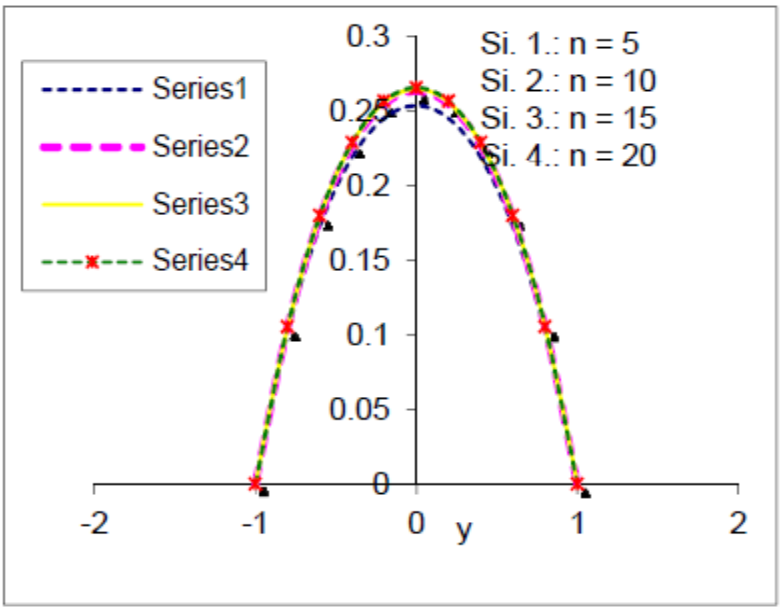

Figure 5: u versus y for M=2(θ = 0^0), Pr=.025, t=1, n=5, 10, 15, 20.

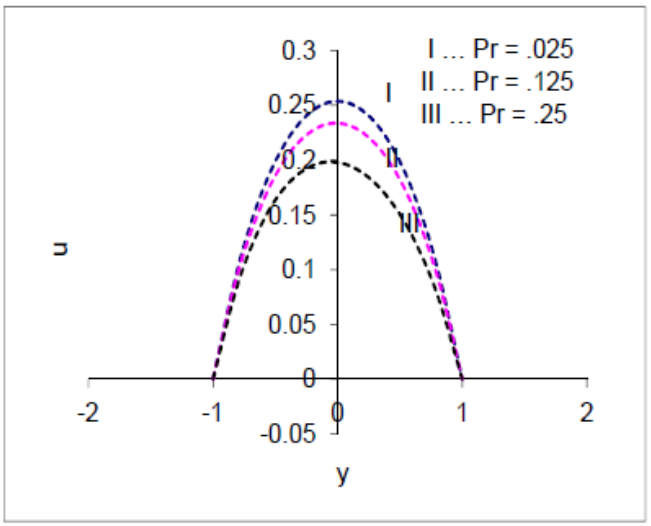

Figure 6: u versus y for M=2(θ = 0^0), n=5, t=1at Pr=.025, .125, .25.

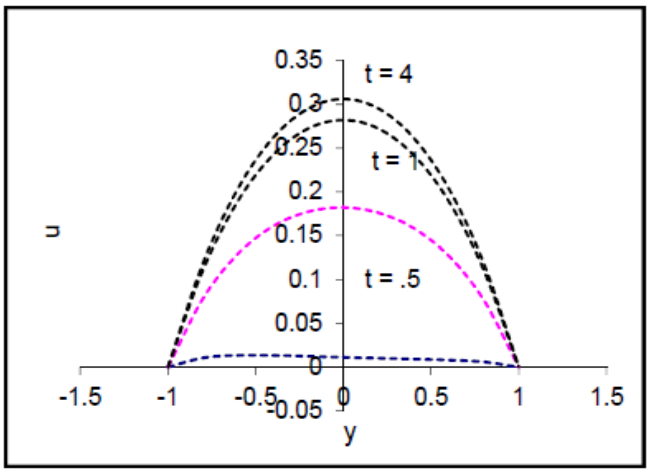

Figure 7: u versus y for M=1.5(θ = 30^0), Pr=.025, n=5 at different time.

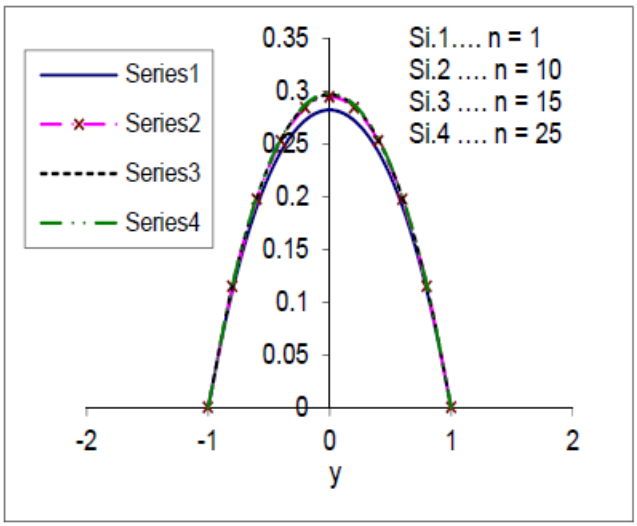

Figure 8: u versus y for M=1.5 (θ = 30^0), Pr=.025, t=1, n=5, 10, 15, 20.

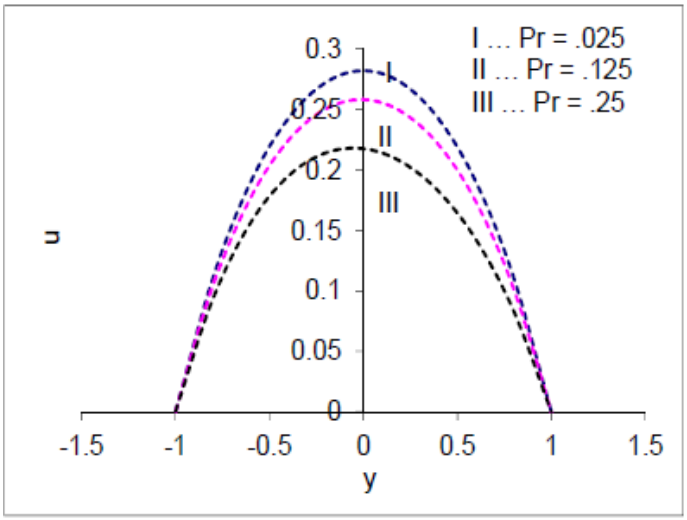

Figure 9: u versus y for M=1.5(θ = 30^0), t=1, n=5, Pr=.025, .125, .25.

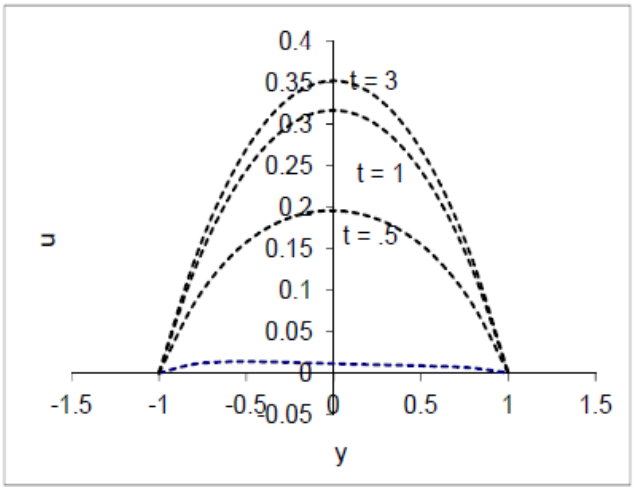

Figure 10: u versus y for M=1(θ = 45^0), Pr=.025, n=5, t=.1, .5, 1, 3

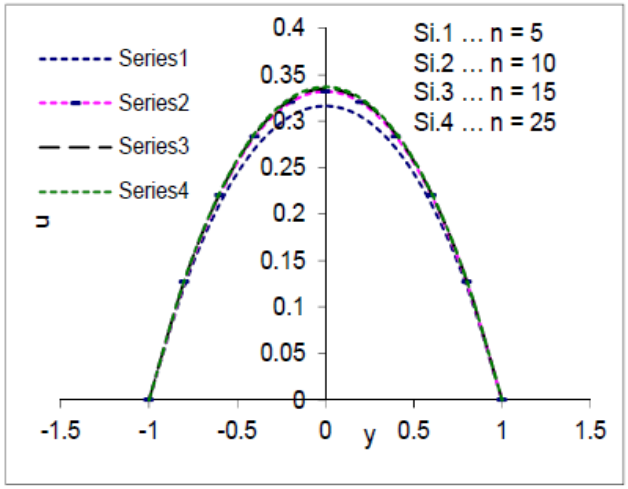

Figure 11: u versus y for M=1(θ = 45^0), Pr=.025, t=1, n=5, 10, 15, 25.

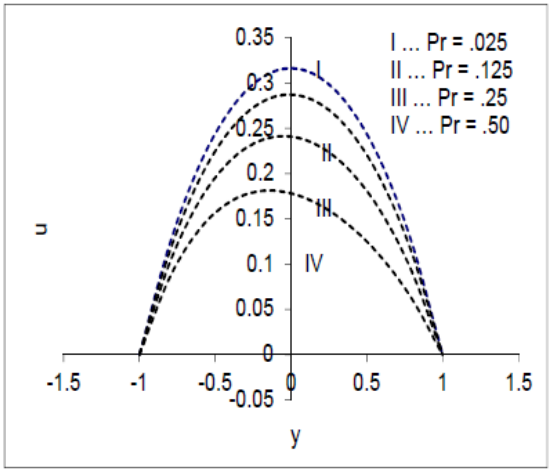

Figure 12: u versus y for M=1(θ = 45^0), t=1, n=5, Pr=.025, .125, .25, .5

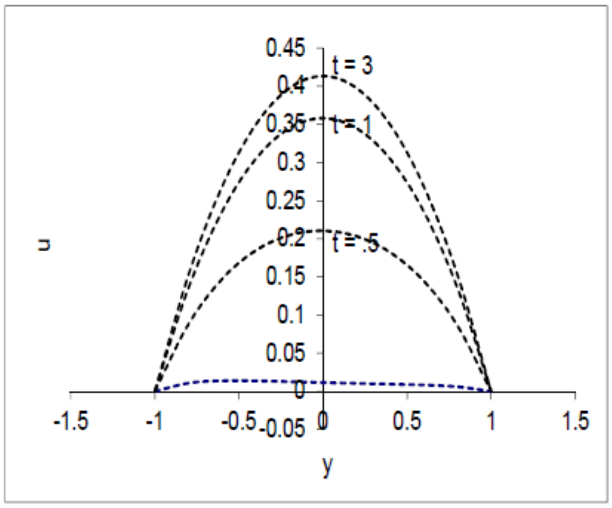

Figure 13: u versus y for M=.5(θ = 60^0), Pr=.025, n=5, t=.1, .5, 1, 3

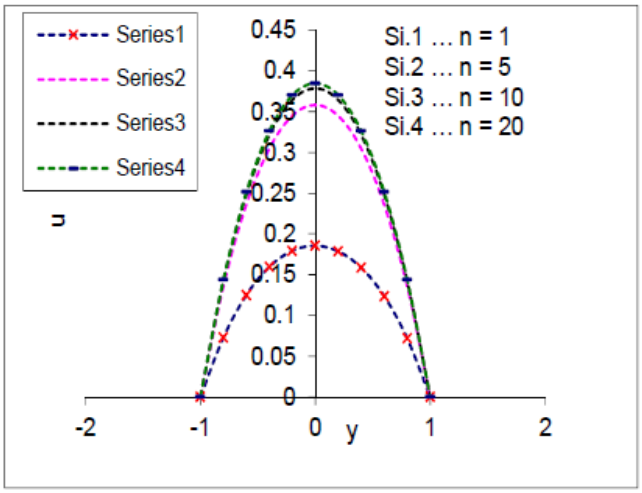

Figure 14: u versus y for M=.5 (θ = 60^0), n=1, 5, 10, 20, t=1, Pr = .025

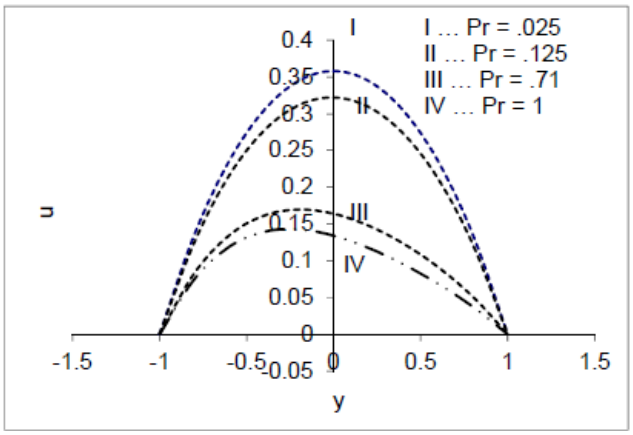

Figure 15: u versus y for M=.5(θ = 60^0), n=5, t=1, Pr =.025, .125, .71, 1.0

In order to prove the accuracy of our numerical results, the present results in steady state at X = 1.0 obtained and considering the modified Grashof number Gr∗L = GrLcosØ, (i.e. the numerical solutions obtained from the equations (9)–(11) are independent of semi vertical angle of the cone Ø) are compared with available similarity solutions in literature. The velocity and temperature profiles of the cone for Pr = 0.72 are displayed in Fig. 2 and the numerical values of local skin-friction τX, temperature T , for different values of Prandtl number are shown in Table 1 are compared with similarity solutions of Lin [9] in steady state using suitable transformation (i.e. Y = (20/9)1/5η, T = (20/9)1/5(−θ(0)), U = (20/9)3/5f′(η), τX = (20/9)2/5f′′(0)). It is observed that the results are in good agreement with each other. It is also noticed that the present results agree well with those of Pop and Watanabe [15], Na and Chiou [12] (as pointed out in Table 1). In Figs. 3–6, transient velocity and temperature profiles are shown at X = 1.0, with various parameters Pr and Ø. The value of t with star (*) symbol denotes the time taken to reach steady state. In Fig. 3, transient velocity profiles are plotted for various values of Ø and Pr = 0.71. When Ø increases near the cone apex, it leads to decrease in the impulsive force along the cone surface. Hence, the difference between temporal maximum velocity values and steady state values decreases with increasing the values of semi vertical angle

Table 1. Comparison of steady state local skin-friction and temperature values at X = 1.0 with those of Lin [9]

	Temperature			Local Skin Friction		
	Lin results [9]		Present results	Lin results [9]		Present results
Pr	-θ(0)	$-\left(\frac{20}{9}\right)^{1/5}\theta(0)$	T	f″ (0)	$\left(\frac{20}{9}\right)^{2/5}f''(0)$	τ_X
0.72	1.52278 1.52278*	1.7864	1.7796	0.88930 0.88930*	1.2240	1.2154
1	1.39174	1.6327 1.6329**	1.6263	0.78446	1.0797	1.0721
2	1.16209	1.3633	1.3578	0.60252	0.8293	0.8235
4	0.98095	1.1508	1.1463	0.46307	0.6373	0.6328
6	0.89195	1.0464	1.0421	0.39688	0.5462	0.5423
8	0.83497	0.9796	0.9754	0.35563	0.4895	0.4859

10	0.79388	0.9314	0.9272	0.32655	0.4494	0.4460
100	0.48372	0.5675	0.5604	0.13371	0.1840	0.1813

of the cone Ø. The tangential component of buoyancy force reduces as the semi vertical angle increases. This causes the velocity to reduce as angle - increases. The momentum boundary layer becomes thick, and the time taken to reach steady state increases for increasing Ø. In Fig. 4, transient temperature profiles are shown for different values of Ø with Pr = 0.71. It is observed the temperature and boundary layer thickness increase with increasing Ø. The difference between temporal maximum temperature values and steady state values decrease with increasing Ø. In Figs. 5 and 6, transient velocity and temperature profiles are plotted for various values of Pr with - = 15^0. Viscous force increases and thermal diffusivity reduces with increasing Pr, causing a reduction in the velocity and temperature as expected. It is observed from the figures that the difference between temporal maximum values and steady state values are reduced when Pr increases. It is also noticed that the time taken to reach steady state increases and thermal boundary layer thickness reduces with increasing Pr.

The study of the effects of the parameters on local as well as the average skin-friction, and the rate of heat transfer is more important in heat transfer problems. The derivatives involved in equations (13) and (14) are obtained using five-point approximation formula and then the integrals are evaluated using Newton-Cotes closed integration formula. The variations of local skin-friction τ_X and local Nusselt number NuX for different values of Ø, at various positions on the surface of the cone (X = 0.25 and 1.0) in the transient period are shown in Figs. 7 and 8 respectively. It is observed from the Fig. 7 that local skin-friction τ_X decreases with increasing Ø, due to the fact that velocity decreases with increasing angle - as shown in Fig. 3 and the influence of - on skin friction τ_X increases as Ø increases in the transient period along the surface of the cone moving away from apex. Fig. 8 reveals that local Nusselt number NuX values decrease with increasing

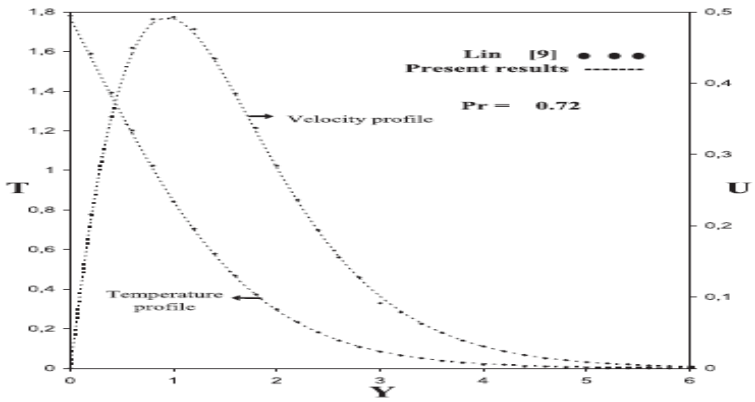

Fig. 2. Comparison of steady state temperature and velocity profiles at X = 1.0.

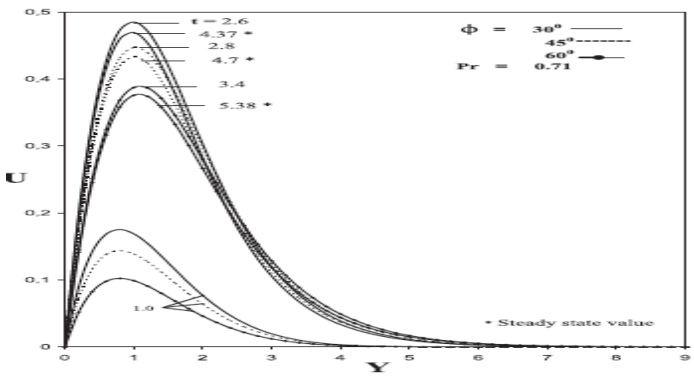

Fig. 3. Transient velocity profiles at X=1.0 for different values of Ø.

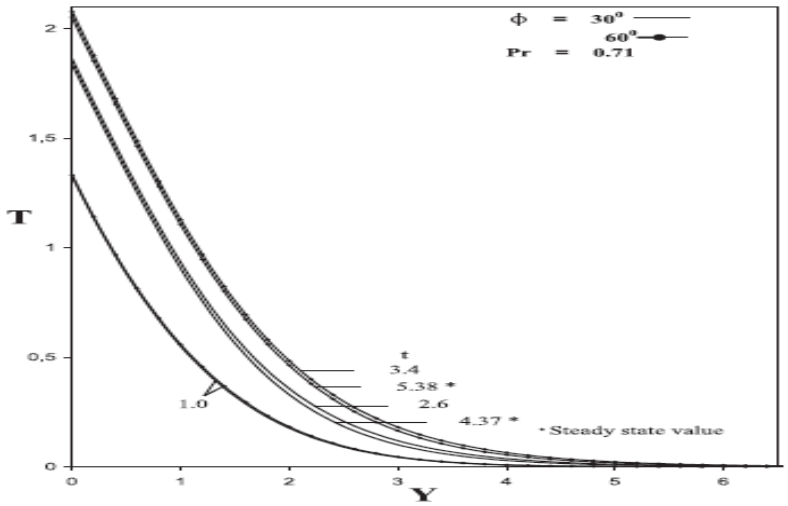

Fig. 4. Transient temperature profiles at X = 1.0 for different values of Ø.

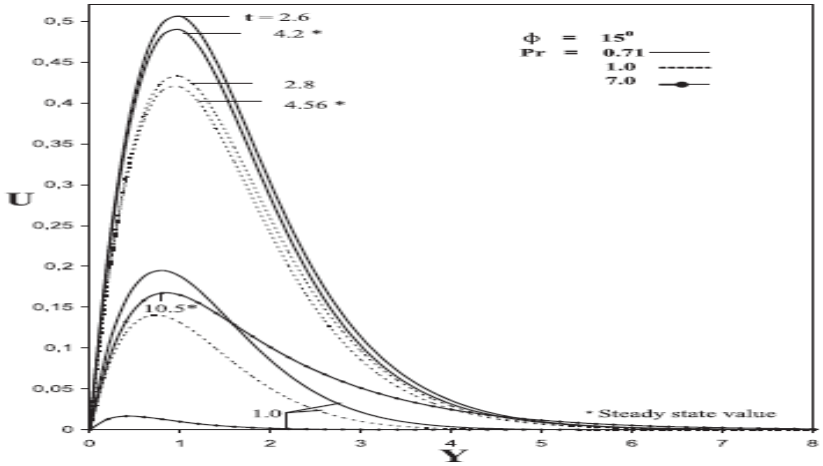

Fig. 5. Transient velocity profiles at X=1.0 for different values of Pr.

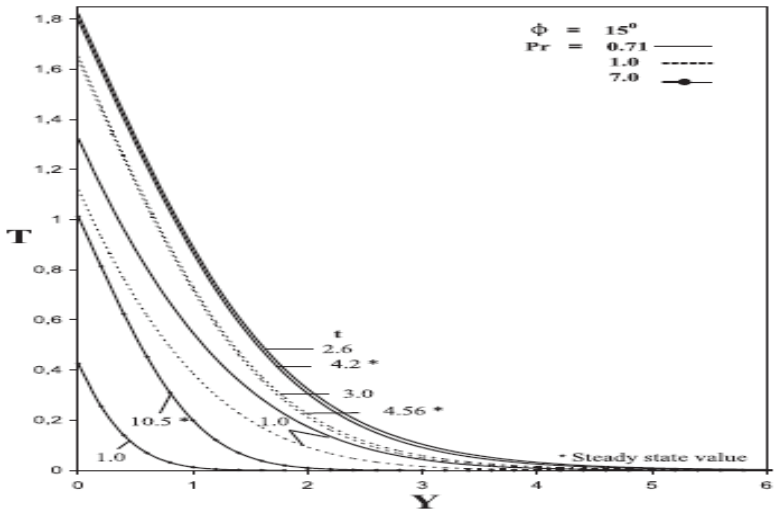

Fig. 6. Transient temperature profiles at X = 1.0 for different values of Pr.

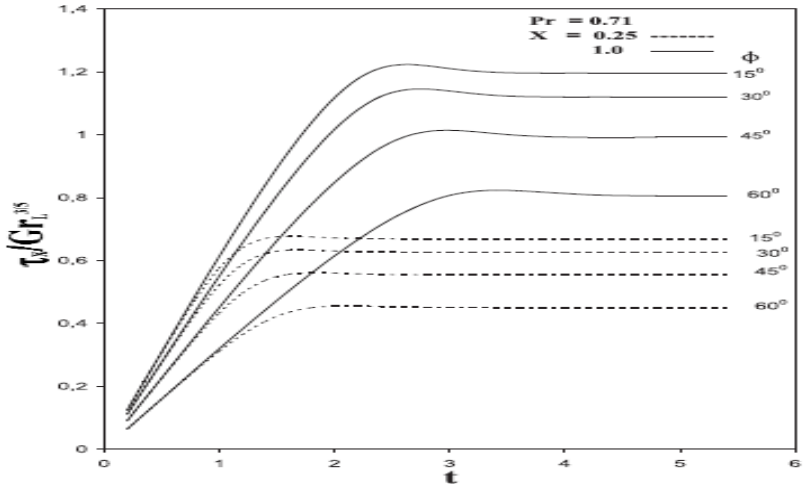

Fig. 7. Local skin friction at X=0.25 and 1.0 for different values of Ø in transient state.

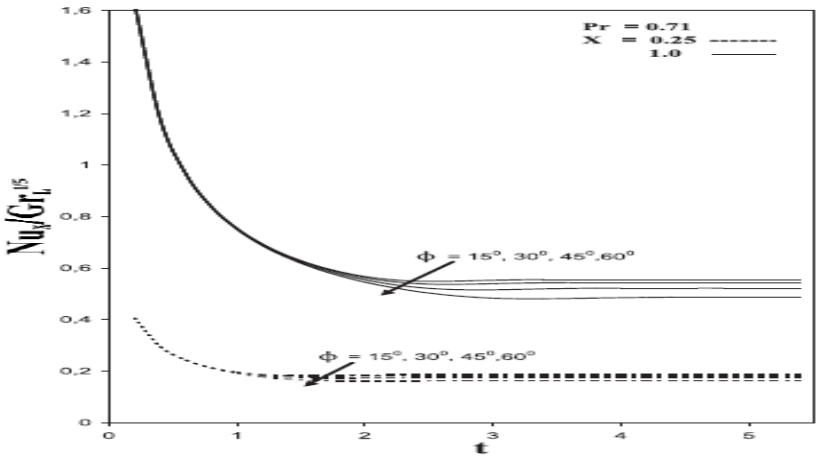

Fig. 8. Local Nusselt number at X = 0.25 and 1.0 for different values of Ø in transient state.

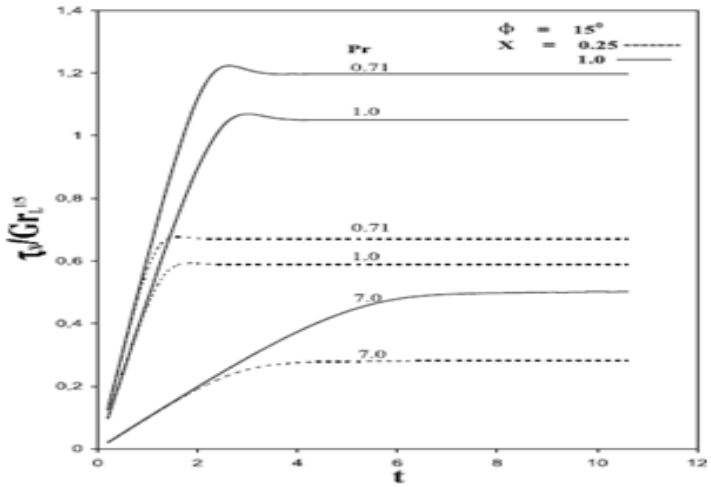

Fig. 9. Local skin friction at X = 0.25 and 1.0 for different values of Pr in transient state.

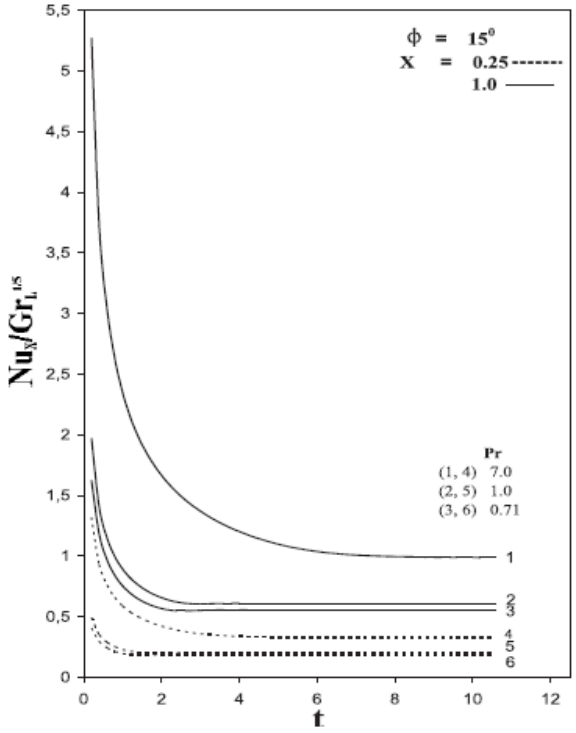

Fig. 10. Local Nusselt number at X=0.25 and 1.0 for different values of Pr in transient state.

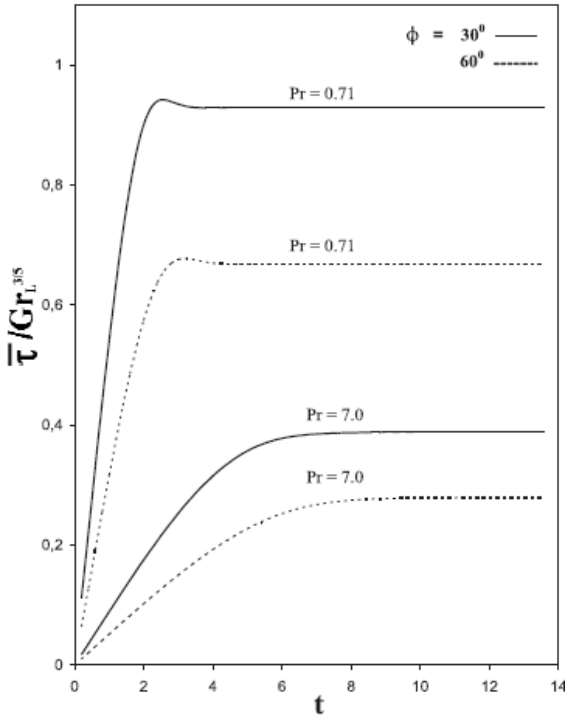

Fig. 11. Average skin friction for different values of Ø and Pr in transient state.

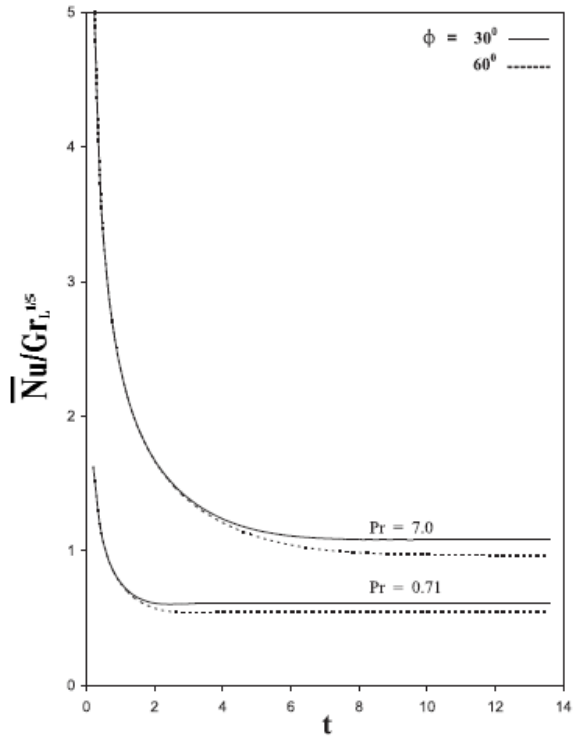

Fig. 12. Average Nusselt number for different values of Ø and Pr in transient state.

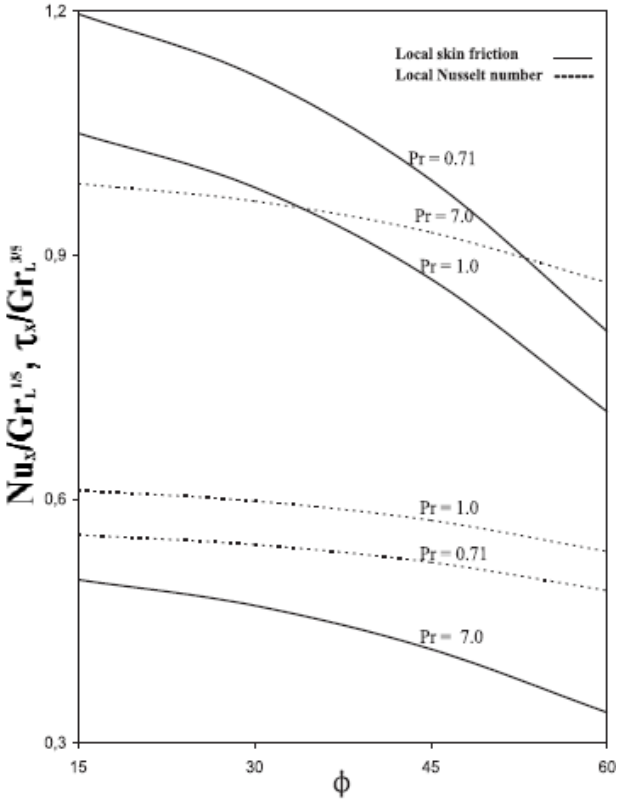

Fig. 13. Local Nusselt number, local skin friction at X = 1.0 for different values of Pr in steady state.

angle Ø as temperature distribution increases with - which is shown in Fig. 4. It is observed that this effect is less near the cone apex. The variation of the local skin-friction τ_X and the local Nusselt number NuX in the transient regime is displayed in Figs. 9 and 10 for different values of Pr and at various positions on the surface of the cone (X = 0.25 and 1.0). The local wall shear stress decreases as Pr increases because velocity decreases with an increasing value of Pr as shown in Fig. 5. In transient period initially local skin friction almost constant through out the surface and gradually increases with time along the surface until it reaches steady state. Local Nusselt number Nu_X increases with increasing Pr and it is clear from the Fig. 10, that decreasing rate of Nu_X increases when the distance increases from the cone vertex along the surface of the cone.

The influence of Ø and Pr on average skin-friction τ transient period are shown in Fig. 11 and it is more for smaller values of angles Ø and lower values of Pr. Fig. 12, displays the influence of average Nusselt number $\overline{Nu}$ in transient period for various values of Pr and Ø. It is clear that $\overline{Nu}$ is more for smaller values of Ø and larger values of Pr. Finally, steady state local skin-friction τ_X and local Nusselt number Nu_X profiles are at X = 1.0 plotted in Fig. 13, against semi vertical angle of the cone Ø for various values of Pr. It is observed that the local shear stress τ_X increases as Pr or Ø decreases, local Nusselt number Nu_X reduces as Ø increases or Pr decreases.

References:

[1] An Introduction to the Theory of Elasticity, R. J. Atkin and N. Fox, Longman, 1980. Math QA931.A78 MATH QA3.M38
[2] Elasticity and plasticity, J. N. Goodier and P. G. Hodge,New York: Wiley, 1958. Math QA931.G6
[3] Elasticity for Engineers, D. S. Dugdale and C. Ruiz, New York: McGraw-Hill, 1971. LSM TA407.D78
[4] Elasticity in Engineering Mechanics, Arthur P. Boresi, Ken P. Chong, New York: Elsevier, 1987. LSM TA405.B67